

Learnability Window in Gated Recurrent Neural Networks

Lorenzo Livi*

February 27, 2026

Abstract

We develop a statistical theory of temporal learnability in recurrent neural networks, showing how gating mechanisms determine the learnability window \mathcal{H}_N , defined as the maximal temporal horizon over which gradient information remains recoverable at sample size N . While classical analyses emphasize numerical stability of Jacobian products, we show that stability alone does not guarantee recoverability. Instead, learnability is governed by the interaction between the decay geometry of the effective learning rate envelope $f(\ell) = \|\mu_{t,\ell}\|_1$, derived from first-order expansions of gate-induced Jacobians in Backpropagation Through Time, and the statistical concentration properties of stochastic gradients. Under heavy-tailed (α -stable) gradient noise, empirical averages concentrate at rate N^{-1/κ_α} with $\kappa_\alpha = \alpha/(\alpha-1)$. We prove that this interaction yields explicit scaling laws for the growth of \mathcal{H}_N , distinguishing logarithmic, polynomial, and exponential temporal learning regimes according to the attenuation of $f(\ell)$. The theory reveals that gate-induced time-scale spectra are the dominant determinants of temporal learnability: broader spectra slow envelope decay and systematically expand \mathcal{H}_N , whereas heavy-tailed noise uniformly compresses temporal horizons by weakening statistical concentration. Empirical results across multiple gated architectures confirm these structural scaling predictions.

1 Introduction

Recurrent neural networks (RNNs) are fundamental models for processing sequential data, yet their ability to learn long-range temporal dependencies remains only partially understood. Gated architectures such as the LSTM and GRU have dramatically improved numerical stability and empirical performance, but it is still unclear which temporal dependencies are statistically recoverable under finite data. Most existing analyses focus on dynamical stability, spectral properties of Jacobian products, or mean-field approximations. These approaches characterize when gradients do not explode or vanish, but they do not provide a statistical criterion for when transported gradient signals remain distinguishable from noise during training. In practice, even stable gradients may be too attenuated or too noisy to carry usable information. Thus, stability alone does not determine temporal learnability.

Our previous work showed that gating induces heterogeneous time scales that shape both state evolution and gradient transport [33]. Here we move beyond dynamical analysis and develop a statistical theory of finite-horizon learnability. The key objects are the effective learning rates $\mu_{t,\ell}$, which quantify how Backpropagation Through Time (BPTT) re-weights gradient signals across time for each neuron and lag. These quantities encode the time-scale spectrum induced by gating and provide a compact description of gradient transport geometry.

The central question addressed in this paper is: given a finite number of training sequences, up to which temporal horizon can dependencies be statistically detected? To answer this, we introduce the *learnability window* \mathcal{H}_N , defined as the largest lag for which gradient information remains recoverable at sample size N . Under heavy-tailed (α -stable) gradient noise, empirical averages concentrate at rate N^{-1/κ_α} with $\kappa_\alpha = \alpha/(\alpha-1)$. We show that the interaction between this concentration rate and the decay geometry of the effective learning rate envelope $f(\ell) = \|\mu_{t,\ell}\|_1$ determines the scaling behavior of \mathcal{H}_N . In particular,

*OPIT – Open Institute of Technology. lorenz.livi@gmail.com. ORCID: 0000-0001-6384-4743. Google Scholar profile.

exponential, polynomial, and logarithmic attenuation of $f(\ell)$ induce qualitatively distinct growth laws for the learnability window, providing a classification of temporal learning regimes.

Although the detectability relation analytically separates envelope geometry and statistical concentration, these mechanisms are dynamically coupled during training. Heavier tails weaken concentration in isolation, but regimes exhibiting slow envelope decay often empirically co-occur with persistent heavy-tailed fluctuations, reflecting the joint evolution of state and parameter dynamics. Thus, heavy-tailed noise does not enhance learnability; rather, it interacts with gate-induced time-scale structure within the same dynamical regime.

This perspective shifts the focus from numerical stability to statistical recoverability. Broad and heterogeneous time-scale spectra slow the decay of $f(\ell)$ and systematically enlarge the learnability window, whereas heavy-tailed gradient noise weakens statistical concentration and therefore counteracts horizon growth. Empirical results across multiple gated RNN architectures confirm these structural predictions.

Contributions. Relative to prior dynamical analyses of gated RNNs, this paper makes four new contributions. (i) We formalize the learnability window \mathcal{H}_N as a finite-sample measure of recoverable temporal dependencies. (ii) We incorporate heavy-tailed (α -stable) gradient noise into the analysis of recurrent training, establishing how non-Gaussian concentration governs detectability. (iii) We derive explicit scaling laws that classify temporal learning regimes according to the decay geometry of the effective learning rate envelope. (iv) We empirically validate these structural scaling predictions across multiple gated architectures.

Paper organization. The remainder of the paper is organized as follows. Section 2 reviews related literature. Section 3 recalls the SGD and BPTT framework. Section 4 derives the effective learning rates for LSTM and GRU. Section 5 develops the theoretical framework of the learnability window. Section 6 presents empirical validation. Section 7 concludes with implications and future directions. Additional technical derivations and supporting analyses are provided in the appendices (Appendices A–I).

2 Related work

The introduction of gating mechanisms in LSTM [19] and GRU [8] was pivotal for controlling temporal credit assignment in recurrent neural networks. Early theoretical works linked the forget gate to an interpretable exponential decay and controllable memory retention [14, 47], while more recent studies connect gating to continuous-time or implicit ODE perspectives [4, 16]. These contributions illuminate how gates shape state dynamics, but do not analyze how gating multiplicative structures affect parameter updates and the capacity for learning long-range dependencies. Our framework bridges that gap by deriving per-lag effective learning rates from products of Jacobians and linking them to finite-horizon learnability.

A complementary line of work models gates as learned rescaling or time-warping mechanisms. Tallec and Ollivier [47] formalized gating as adaptive time dilation, and recent geometry-based analyses [28] study how gating choices influence information flow. We build on these ideas by explicitly casting gate-derived Jacobian terms into effective learning rates and embedding them in detectability bounds via mutual information / Fano theory.

The classical vanishing/exploding gradients problem motivated many stabilization techniques: clipping, spectral regularization, and orthogonality or unitary RNNs [1, 3, 24, 39, 50]. Hierarchical, dilated, or skip architectures shorten propagation paths [5, 9, 26], while continuous-time and neural ODE approaches enhance stability and expressivity [17, 41]. Works on orthogonal / dynamical isometry control the conditioning of gradient transport [6, 40] but do not address whether transported gradients still carry statistically reliable information over long lags. In contrast, we analyze statistical detectability, showing that even when products of Jacobians remain numerically stable, learning can be ineffective if the envelope decays too rapidly. Related difficulties have long been observed in tasks with delayed supervision or rewards [3], where the learning signal must be propagated across long temporal gaps; however, existing analyses typically focus on optimization stability rather than statistical detectability across lags.

A related but distinct line of work concerns memory capacity in reservoir computing and echo state networks, where the recurrent dynamics are kept fixed and only a readout layer is trained [12, 22, 49]. In this setting, classical results characterize the ability of a randomly driven recurrent system to retain information about past inputs over time, typically quantified via linear or nonlinear memory capacity measures. Such analyses focus on expressivity and information retention properties of untrained dynamical systems, rather than on the optimization dynamics of recurrent weights under gradient-based learning. By contrast, the present work addresses a complementary question: how training dynamics themselves impose horizon-dependent limits on learnability through the interaction between temporal Jacobian transport, effective learning rates, and noise. In particular, our framework does not rely on fixed reservoirs, but instead characterizes how credit assignment and detectability degrade under heavy-tailed gradient noise, limiting the realizable horizon even in architectures with sufficient representational capacity.

In the broader learning systems literature, trainability has been studied via mean-field theory, spectral initialization, curvature, and the geometry of parameter landscapes [10, 25, 29, 31, 35, 40, 43, 44, 52, 53]. In recurrent and transformer settings, recent work further links trainability to Jacobian spectra, Fisher information, and anisotropic learning rates [2, 13, 46, 51]. Related analyses study gradient signal-to-noise ratios and noise scales as a function of batch size, curvature, and optimizer dynamics, with the aim of understanding optimization efficiency and generalization behavior [23, 36]. However, these approaches treat gradients as local-in-time objects and do not account for the temporal transport inherent in recurrent learning, where gradient signals must be propagated across time through products of Jacobians. Zhou et al. [54] investigate the generalization gap between stochastic gradient descent (SGD) and Adam, attributing Adam’s performance to a sharpness reduction effect caused by adaptive coordinate-wise scaling and noting an inherent clipping behavior. Our framework is complementary: it provides a finite-horizon, sample-complexity view anchored in transported gradient statistics, showing how the tail behavior of gradient noise and gate structure jointly determine which temporal lags are statistically learnable.

Simsekli et al. [45] show that mini-batch SGD noise often exhibits α -stable, heavy-tailed behavior rather than Gaussian tails. Subsequent research has further examined the algorithmic and theoretical consequences of such heavy-tailed gradient statistics. Hübler et al. [20] establish a unified framework connecting gradient clipping and normalization, proving that both act as implicit variance control mechanisms for α -stable noise and can stabilize training without sacrificing convergence speed. Finally, Liu and He [32] extend these ideas to online convex optimization with heavy-tailed stochastic gradients, providing convergence guarantees and adaptive algorithms that remain stable even when gradient moments of order two do not exist. In our work, we adopt the empirical reality of heavy-tailed gradient noise as a basic modeling premise.

Finally, structured state-space models achieve long-range dependencies via implicit recurrence or convolutional kernels [15, 16]. Our focus remains on classical recurrent systems trained by BPTT: we deliver measurable per-lag detection thresholds and learnability windows backed by heavy-tailed gradient statistics.

3 Backpropagation through time

Training RNNs follows the same fundamental principle as feedforward models: parameter updates are obtained through SGD or variations thereof [42]. Given trainable parameters θ and learning rate μ , the update at iteration r is

$$\theta_{r+1} = \theta_r - \mu \nabla_{\theta} \mathcal{L}(\theta_r), \quad \mathcal{L} = \sum_{t=1}^T \mathcal{E}_t, \quad (1)$$

where \mathcal{E}_t denotes the instantaneous loss at time t within a sequence of length T . In recurrent architectures, however, computing the gradient $\nabla_{\theta} \mathcal{L}$ requires unrolling the network dynamics through time and accounting for how earlier states influence later losses—a process known as Backpropagation Through Time.

Let s_t denote the recurrent state. The total gradient of the loss with respect to the parameters can be written as

$$\nabla_{\theta} \mathcal{L} = \sum_{t=1}^T \frac{\partial \mathcal{E}_t}{\partial \theta} = \sum_{t=1}^T \frac{\partial \mathcal{E}_t}{\partial s_t} \sum_{\ell=1}^t \frac{\partial s_t}{\partial s_{\ell}} \frac{\partial s_{\ell}}{\partial \theta}. \quad (2)$$

The outer sum aggregates contributions from all time steps, while the inner chain rule expresses how parameter perturbations at earlier times influence the current loss through the recurrent dynamics. To make this dependence explicit, define $J_j = \frac{\partial s_j}{\partial s_{j-1}}$ and $B_\ell(\theta) = \frac{\partial s_\ell}{\partial \theta}$. Here J_j is the state Jacobian, which quantifies how the state evolves in response to infinitesimal perturbations of the previous state, and $B_\ell(\theta)$ is the parameter-state Jacobian, measuring the instantaneous sensitivity of the state to the parameters at step ℓ . Substituting these definitions into Eq. (2), the gradient contribution of a specific loss term \mathcal{E}_t becomes

$$\frac{\partial \mathcal{E}_t}{\partial \theta} = \delta_t^\top \sum_{\ell=1}^t \mathcal{M}_{t,\ell} B_\ell(\theta), \quad \mathcal{M}_{t,\ell} := \prod_{j=\ell+1}^t J_j, \quad (3)$$

where $\delta_t = \partial \mathcal{E}_t / \partial s_t$ denotes the local loss gradient at time t . The matrix product $\mathcal{M}_{t,\ell}$, often referred to as the state-transition Jacobian product, transports this signal backward through the sequence, modulating both its magnitude and direction as it interacts with the intermediate state Jacobians J_j .

4 Effective learning rates for LSTM and GRU

This section derives, for LSTM and GRU, the per-neuron, per-lag effective learning rates obtained via a first-order expansion of Jacobian products first introduced in [33] and briefly described in Appendix A. Together with the BPTT decomposition in Sec. 3, these rates connect state-space multiplicative geometry (gates) with parameter-space learning dynamics, and form the basis of the learnability analysis in Sec. 5.

4.1 General notation and conventions

Let $x_t \in \mathbb{R}^D$ be the input at step t , $h_t \in \mathbb{R}^H$ the hidden state, and (for LSTM) $c_t \in \mathbb{R}^H$ the cell state. For any $v \in \mathbb{R}^H$, let $D(v) := \text{diag}(v) \in \mathbb{R}^{H \times H}$. Hadamard (elementwise) product is \odot . The logistic and hyperbolic tangent are elementwise: $\sigma(\cdot)$ and $\tanh(\cdot)$. We use the diagonal ‘‘slope’’ matrices

$$S^\sigma(u) := D(\sigma'(u)), \quad S^{\tanh}(u) := D(1 - \tanh^2(u)).$$

When convenient, $D(h_{t-1})$ is abbreviated by $D_{h,t-1}$. Weight matrices have shapes $W_\bullet \in \mathbb{R}^{H \times D}$, $U_\bullet \in \mathbb{R}^{H \times H}$, and $b_\bullet \in \mathbb{R}^H$.

Throughout, one-step Jacobians are derivatives with respect to the previous state: for LSTM we stack $s_t = [h_t; c_t] \in \mathbb{R}^{2H}$ and write $J_t = \partial s_t / \partial s_{t-1} \in \mathbb{R}^{2H \times 2H}$; for GRU, $J_t = \partial h_t / \partial h_{t-1} \in \mathbb{R}^{H \times H}$.

For a square $A \in \mathbb{R}^{n \times n}$, $\text{diagvec}(A) \in \mathbb{R}^n$ is the vector formed by the diagonal of A . In LSTM, when $\mathcal{M}_{t,\ell} = \prod_{j=\ell+1}^t J_j$ is written in $2H \times 2H$ block form for $s = [h; c]$, the notation $[\cdot]_{h,c} \in \mathbb{R}^{H \times H}$ refers to the top-right block mapping $c_\ell \mapsto h_t$.

4.2 LSTM: one-step Jacobian and effective learning rates

Dynamics. An LSTM maintains (h_t, c_t) and computes

$$a_t^i = W_i x_t + U_i h_{t-1} + b_i, \quad i_t = \sigma(a_t^i), \quad (\text{input gate}) \quad (4)$$

$$a_t^f = W_f x_t + U_f h_{t-1} + b_f, \quad f_t = \sigma(a_t^f), \quad (\text{forget/retention}) \quad (5)$$

$$a_t^o = W_o x_t + U_o h_{t-1} + b_o, \quad o_t = \sigma(a_t^o), \quad (\text{output/expression}) \quad (6)$$

$$a_t^g = W_g x_t + U_g h_{t-1} + b_g, \quad g_t = \tanh(a_t^g), \quad (\text{cell candidate}) \quad (7)$$

$$c_t = f_t \odot c_{t-1} + i_t \odot g_t, \quad h_t = o_t \odot \tanh(c_t). \quad (8)$$

Define the diagonal gate matrices and slopes

$$F_t = D(f_t), \quad I_t = D(i_t), \quad O_t = D(o_t), \quad G_t = D(g_t), \quad S_t^i = S^\sigma(a_t^i), \quad S_t^f = S^\sigma(a_t^f), \quad S_t^o = S^\sigma(a_t^o), \quad S_t^g = S^{\tanh}(a_t^g),$$

and cell-expression factors

$$S_t := S^{\tanh}(c_t) = D(1 - \tanh^2(c_t)), \quad H_t := D(\tanh(c_t)), \quad E_t := D(o_t \odot (1 - \tanh^2(c_t))) = O_t S_t.$$

One-step Jacobian. With $s_t = [h_t; c_t]$, the Jacobian blocks are

$$\frac{\partial c_t}{\partial c_{t-1}} = F_t, \quad \frac{\partial c_t}{\partial h_{t-1}} = \underbrace{D(c_{t-1}) S_t^f U_f}_{\text{via forget}} + \underbrace{I_t S_t^g U_g}_{\text{via candidate}} + \underbrace{G_t S_t^i U_i}_{\text{via input}} =: C_t^{(h)}, \quad (9)$$

$$\frac{\partial h_t}{\partial c_{t-1}} = E_t F_t, \quad \frac{\partial h_t}{\partial h_{t-1}} = H_t S_t^o U_o + E_t C_t^{(h)}. \quad (10)$$

Collecting terms,

$$J_t = \begin{bmatrix} H_t S_t^o U_o + E_t C_t^{(h)} & E_t F_t \\ C_t^{(h)} & F_t \end{bmatrix} \in \mathbb{R}^{2H \times 2H}. \quad (11)$$

First-order expansion of the transport. Let $\mathcal{M}_{t,\ell} = \prod_{j=\ell+1}^t J_j$. Decompose $J_t = T_t + R_t$ with

$$T_t = \begin{bmatrix} 0 & E_t F_t \\ 0 & F_t \end{bmatrix}, \quad R_t := J_t - T_t,$$

so T_t contains *retention* (F_t) and *expression* (E_t) along the cell path, while R_t collects recurrently mixed corrections. By the first-order product rule,

$$\mathcal{M}_{t,\ell} \approx T_{t,\ell} + \sum_{p=\ell+1}^t T_{t,p} R_p T_{p-1,\ell}, \quad T_{a:b} := \prod_{j=b+1}^a T_j, \quad T_{b:b} := I. \quad (12)$$

Since the loss depends on h_t (Sec. 3), only the top-right block of $\mathcal{M}_{t,\ell}$ (mapping $c_\ell \mapsto h_t$) contributes directly to the gradient transport.

Zeroth-order contributions. Because T_t is block upper-triangular with a zero $h \rightarrow h$ block, the (h, c) block of the transport $T_{t,\ell} := \prod_{j=\ell+1}^t T_j$ reduces to a single surviving path in which the signal remains in the cell state until time t :

$$[T_{t,\ell}]_{h,c} = E_t \Phi_{t,\ell}, \quad \Phi_{a:b} := \prod_{j=b+1}^a F_j, \quad \Phi_{b:b} = I.$$

In particular, the $c \rightarrow h$ transition can occur only at the final time t . Extracting the diagonal gives the neuron-wise rates

$$\gamma_{t,\ell}^{(0)} := \text{diagvec}(E_t \Phi_{t,\ell}) \in \mathbb{R}^H, \quad \gamma_{t,\ell}^{(0,q)} = e_{t,q} \prod_{j=\ell+1}^t f_{j,q}, \quad e_{t,q} = o_{t,q} (1 - \tanh^2(c_{t,q})). \quad (13)$$

First-order diagonal correction. From the first-order product expansion (12), the contribution of a single recurrent mixing insertion to the top-right block of the transport is

$$\gamma_{t,\ell}^{(1)} := \sum_{p=\ell+1}^t \text{diagvec}([T_{t,p} R_p T_{p-1,\ell}]_{h,c}) \in \mathbb{R}^H,$$

where $[\cdot]_{h,c}$ denotes the $H \times H$ block mapping $c_\ell \mapsto h_t$. Unlike the zeroth-order case, the presence of the recurrent correction R_p reintroduces $h \rightarrow h$ transport, allowing a single mixing event to occur at any intermediate time $p \in \{\ell+1, \dots, t\}$. This term therefore collects the diagonal components of the first-order Fréchet expansion in Appendix A, corresponding to neuron-wise self-couplings induced by a single insertion of the recurrent mixing blocks. Off-diagonal entries encode cross-neuron interactions and are intentionally discarded, as they do not admit a neuron-wise time-scale interpretation.

LSTM effective learning rates. With global learning rate $\mu > 0$, we define the per-lag, per-neuron effective learning rates

$$\mu_{t,\ell} := \mu(\gamma_{t,\ell}^{(0)} + \gamma_{t,\ell}^{(1)}) \in \mathbb{R}^H, \quad \mu_{t,\ell}^{(q)} = \mu(\gamma_{t,\ell}^{(0,q)} + \gamma_{t,\ell}^{(1,q)}). \quad (14)$$

These quantities act as scalar multipliers that modulate the contribution of gradients originating at lag $(t-\ell)$ to parameter updates, providing a neuron-wise characterization of the effective learning dynamics induced by the LSTM gates.

4.3 GRU: one-step Jacobian and effective learning rates

Dynamics. A GRU updates

$$a_t^z = W_z x_t + U_z h_{t-1} + b_z, \quad z_t = \sigma(a_t^z) \quad (\text{update/leak}) \quad (15)$$

$$a_t^r = W_r x_t + U_r h_{t-1} + b_r, \quad r_t = \sigma(a_t^r) \quad (\text{reset/filtering}) \quad (16)$$

$$a_t^g = W_h x_t + U_h (r_t \odot h_{t-1}) + b_h, \quad g_t = \tanh(a_t^g) \quad (\text{candidate}) \quad (17)$$

$$h_t = (1 - z_t) \odot h_{t-1} + z_t \odot g_t. \quad (18)$$

Let $Z_t = D(z_t)$, $R_t = D(r_t)$, $G_t = D(g_t)$, $D_{h,t-1} = D(h_{t-1})$ and $S_t^z = S^\sigma(a_t^z)$, $S_t^r = S^\sigma(a_t^r)$, $S_t^g = S^{\tanh}(a_t^g)$.

One-step Jacobian. Differentiating the leak and update paths gives

$$\frac{\partial}{\partial h_{t-1}}[(1 - z_t) \odot h_{t-1}] = (I - Z_t) - D_{h,t-1} S_t^z U_z, \quad (19)$$

$$\frac{\partial g_t}{\partial h_{t-1}} = S_t^g U_h (R_t + D_{h,t-1} S_t^r U_r), \quad (20)$$

$$\frac{\partial}{\partial h_{t-1}}[z_t \odot g_t] = G_t S_t^z U_z + Z_t \frac{\partial g_t}{\partial h_{t-1}}. \quad (21)$$

Summing contributions,

$$J_t = (I - Z_t) + (G_t - D_{h,t-1}) S_t^z U_z + Z_t S_t^g U_h R_t + Z_t S_t^g U_h D_{h,t-1} S_t^r U_r. \quad (22)$$

First-order expansion of the transport. Write the Jacobian as $J_t = T_t + \mathcal{R}_t$, where

$$T_t := I - Z_t$$

is the diagonal retention operator induced by the update gate, and \mathcal{R}_t collects all remaining recurrent mixing terms. For the transport $\mathcal{M}_{t,\ell} = \prod_{j=\ell+1}^t J_j$, a first-order expansion yields

$$\mathcal{M}_{t,\ell} \approx \Phi_{t:\ell} + \sum_{p=\ell+1}^t \Phi_{t:p} \mathcal{R}_p \Phi_{p-1:\ell}, \quad \Phi_{t:\ell} := \prod_{j=\ell+1}^t (I - Z_j), \quad \Phi_{\ell:\ell} = I. \quad (23)$$

Zeroth-order contributions. The diagonal product $\Phi_{t:\ell}$ yields the primary leak/retention envelope

$$\gamma_{t,\ell}^{(0)} = \text{diagvec}(\Phi_{t:\ell}) \in \mathbb{R}^H, \quad \gamma_{t,\ell}^{(0,q)} = \prod_{j=\ell+1}^t (1 - z_{j,q}), \quad (24)$$

which governs the zeroth-order neuron-wise time scales associated with the update gate.

In addition, the multiplicative action of the reset gate along the candidate pathway induces further diagonal attenuations that are useful to track explicitly. We therefore define the diagonal pathwise envelopes

$$\rho_{t,\ell}^{(0,q)} = \prod_{j=\ell+1}^t r_{j,q}, \quad \eta_{t,\ell}^{(0,q)} = \prod_{j=\ell+1}^t (1 - z_{j,q}) r_{j,q}, \quad (25)$$

which capture pure reset attenuation and mixed update-reset attenuation, respectively. These quantities isolate the shrinkage associated with reset-controlled chains and are reported as complementary diagonal envelopes, rather than as additional terms in the strict $T_t + \mathcal{R}_t$ product expansion.

First-order diagonal correction. The first-order diagonal correction associated with recurrent mixing is obtained by extracting the diagonal of the first-order term in (23):

$$\gamma_{t,\ell}^{(1)} := \sum_{p=\ell+1}^t \text{diagvec}(\Phi_{t:p} \mathcal{R}_p \Phi_{p-1:\ell}) \in \mathbb{R}^H.$$

This term collects the diagonal components arising from a single insertion of the recurrent mixing operator into an otherwise gate-diagonal transport. As in the LSTM case, off-diagonal components encode cross-neuron interactions and are intentionally discarded in order to preserve a neuron-wise time-scale interpretation.

GRU effective learning rates. With global learning rate $\mu > 0$, we define the per-lag, per-neuron effective learning rates as

$$\mu_{t,\ell}^{(q)} := \mu \left(\gamma_{t,\ell}^{(0,q)} + \rho_{t,\ell}^{(0,q)} + \eta_{t,\ell}^{(0,q)} + \gamma_{t,\ell}^{(1,q)} \right), \quad q = 1, \dots, H. \quad (26)$$

These quantities provide a diagonal, neuron-wise summary of how update and reset gates jointly shape the effective learning dynamics across temporal lags.

4.4 Considerations in terms of optimization dynamics

The effective learning rates quantify how gates re-weight BPTT contributions at lag $(t-\ell)$ on a per-neuron basis, even under a fixed global learning rate μ in SGD-like optimizers. Zeroth-order terms produce diagonal contributions, while the full definition of the first-order terms introduce anisotropy: the recurrent matrices modulated by gate slopes mix coordinates and steer updates into privileged subspaces. As a result, gated RNNs act as implicit *multi-rate optimizers*: they set heterogeneous, lag-dependent learning rates across neurons and selectively bias update directions. This interpretation of gates as multi-rate optimizers was initially discovered in [33] for the gated RNN models in Appendix B.

5 Learnability from effective learning rates under heavy-tailed gradient noise

In this section, we quantify finite-horizon learnability. Starting from the per-lag, per-neuron effective learning rates $\mu_{t,\ell}^{(q)}$, we cast lag- ℓ credit assignment as a binary detection problem on a matched statistic built from BPTT. We then model the fluctuations of this statistic with a symmetric α -stable (S α S) location family, justify information-theoretic lower bounds via local asymptotic normality for $\alpha > 1$, and translate them into sample complexity requirements and a learnability window \mathcal{H}_N . Finally, we derive scaling laws for \mathcal{H}_N under logarithmic, polynomial, and exponential decay of the envelope $f(\ell) := \|\mu_{t,\ell}\|_1 = \sum_{q=1}^H |\mu_{t,\ell}^{(q)}|$, highlighting the role of the tail index α .¹

¹Throughout, we suppress the explicit dependence on the time index t in quantities such as $f(\ell)$ and $m_q(\ell)$. In the theoretical development, t is fixed and plays no role beyond anchoring the starting point of the Jacobian product. In the empirical evaluation,

5.1 Setup and link to BPTT

We begin by isolating the portion of the BPTT gradient that reflects the influence of past states. Throughout this section, we fix a reference time t and interpret $\ell \geq 1$ as a backward temporal displacement (lag) relative to t . All quantities indexed by (t, ℓ) refer to contributions originating from the state at lag ℓ prior to time t . We assume ℓ does not exceed the available history.

Let s_t denote the recurrent state used by BPTT (Sec. 3); for LSTM, $s_t = [h_t; c_t]$, whereas for GRU and gated RNNs in Appendix B, $s_t = h_t$.

Recalling the one-step decomposition in Eq. (3), we isolate the lag- ℓ contribution to the current gradient. Define

$$g_{t,\ell}(\theta) := \delta_t^\top \mathcal{M}_{t,\ell} B_{t,\ell}(\theta) \in \mathbb{R}^{1 \times P}, \quad (27)$$

where $\delta_t = \partial \mathcal{L}_t / \partial s_t$ is the local loss gradient, $\mathcal{M}_{t,\ell}$ denotes the ℓ -step Jacobian product transporting perturbations across a temporal displacement of ℓ steps, and $B_{t,\ell}(\theta)$ is the parameter Jacobian associated with the state at lag ℓ . The vector $g_{t,\ell}(\theta)$ represents the lag- ℓ contribution to the BPTT gradient in parameter space.

Following the first-order approximation introduced in Appendix A, we approximate the Jacobian product by a diagonal operator collecting only neuronwise effective learning rates:

$$\mathcal{M}_{t,\ell} \approx \text{diag}(\mu_{t,\ell}^{(1)}, \dots, \mu_{t,\ell}^{(H)}),$$

where $\mu_{t,\ell}^{(q)} \geq 0$ quantifies the cumulative modulation induced by gating along the ℓ -step path associated with neuron q .

Decomposing the parameter Jacobian associated with lag ℓ into neuronwise blocks,

$$B_{t,\ell}(\theta) = [B_{t,\ell}^{(1)} \ \dots \ B_{t,\ell}^{(H)}], \quad B_{t,\ell}^{(q)} \in \mathbb{R}^{1 \times P},$$

the lag- ℓ gradient contribution admits the following vector-valued first-order approximation of Eq. (27),

$$g_{t,\ell}(\theta) \approx \sum_{q=1}^H \mu_{t,\ell}^{(q)} \delta_t^{(q)} B_{t,\ell}^{(q)}(\theta), \quad (28)$$

where $\delta_t^{(q)}$ denotes the q -th component of the local loss gradient at time t .

Equation (28) makes explicit that the lag- ℓ contribution to the parameter gradient is a vector obtained by summing neuronwise parameter sensitivities, each modulated by a corresponding effective learning rate. Thus, BPTT transports gradients along multiplicative chains of effective learning rate values, while the geometric structure of the parameter Jacobian determines how this transported signal is distributed across parameters.

5.2 Binary detection and matched statistic

We formalize finite-horizon learnability by asking when information about a state at lag ℓ remains statistically present in the stochastic gradient at time t . As shown in Sec. 5.1, the lag- ℓ contribution to the BPTT gradient is, up to first-order approximation, the vector $g_{t,\ell}(\theta) \in \mathbb{R}^{1 \times P}$ defined in Eq. (28).

To assess whether such information is recoverable in finite samples, we cast lag- ℓ learnability as a *binary detection problem*: from the noisy gradient contribution $g_{t,\ell}(\theta)$, can we statistically distinguish the presence of a nonzero expected signal from the case where no such contribution exists? In principle, this detection problem could be formulated directly in the P -dimensional parameter space. However, working with a unidimensional statistic substantially simplifies both the statistical analysis and the interpretation of finite-sample effects, while preserving the relevant signal-to-noise structure.

we average $\mu_{t,\ell}$ over all valid t and all diagnostic sequences, so that only the lag dependence ℓ remains. In both cases, the learnability analysis depends solely on how these functionals vary with ℓ , not on their absolute position along the sequence.

We therefore compress the vector-valued quantity $g_{t,\ell}(\theta)$ into a scalar by applying a fixed linear readout. Let $w \in \mathbb{R}^P$ be a random unit-norm vector, drawn independently of the data and fixed throughout training and across all model instances. This projection defines a one-dimensional observable that can be interpreted as a random but unbiased probe of the gradient geometry.

Applying this readout to $g_{t,\ell}(\theta)$ and using the first-order approximation Eq. (28), we obtain the scalar neuronwise alignment variables

$$\zeta_{t,\ell}^{(q)} := \delta_t^{(q)} \langle B_{t,\ell}^{(q)}(\theta), w \rangle, \quad (29)$$

so that the lag- ℓ contribution reduces to the weighted sum $\sum_{q=1}^H \mu_{t,\ell}^{(q)} \zeta_{t,\ell}^{(q)}$.

Because the same realization of w is used for all models and training runs, differences in detectability across architectures reflect differences in temporal credit assignment and gradient transport, rather than artifacts of the projection itself. Moreover, since w is drawn uniformly from the unit sphere, its distribution is rotationally invariant. As a result, the projection $\langle B_{t,\ell}^{(q)}(\theta), w \rangle$ provides an unbiased random probe of the typical magnitude and relative alignment of the neuronwise parameter-sensitivity directions, without privileging any fixed parameter direction.

The scalar variables $\zeta_{t,\ell}^{(q)}$ quantify how the transported gradient components associated with neuron q align, through the parameter Jacobian, with the fixed readout direction w . The effective learning rates $\mu_{t,\ell}^{(q)}$ weight these alignment terms and thus govern how strongly each lag influences parameter updates.

Framed this way, the question of whether RNNs can use BPTT to exploit a dependency at lag ℓ becomes a question of *detectability*: is the signal induced by the state at lag ℓ large enough, relative to gradient noise, to remain statistically distinguishable? This viewpoint allows us to apply information-theoretic tools to characterize when past states remain recoverable during training.

Define the expected alignment $m_q(\ell) = \mathbb{E}[\zeta_{t,\ell}^{(q)}]$ and construct a matched statistic that aggregates lag- ℓ evidence across neurons:

$$S_{t,\ell} = \sum_{q=1}^H \mu_{t,\ell}^{(q)} \operatorname{sgn}(m_q(\ell)) \zeta_{t,\ell}^{(q)}. \quad (30)$$

The factor $\operatorname{sgn}(m_q(\ell))$ flips each coordinate so that its contribution is oriented along the direction of its expected alignment. Consequently, under the data distribution, $\operatorname{sgn}(m_q(\ell)) \zeta_{t,\ell}^{(q)}$ has nonnegative mean, and every term in the sum contributes constructively.²

Taking expectations over the randomness of the data yields

$$\mathbb{E}[S_{t,\ell}] = \sum_{q=1}^H \mu_{t,\ell}^{(q)} |m_q(\ell)| = \bar{m}_\mu(\ell) f(\ell), \quad (31)$$

where

$$\bar{m}_\mu(\ell) := \frac{\sum_{q=1}^H \mu_{t,\ell}^{(q)} |m_q(\ell)|}{\sum_{q=1}^H |\mu_{t,\ell}^{(q)}|} \quad (32)$$

is an envelope-normalized alignment coefficient aggregating the neuronwise magnitudes $|m_q(\ell)|$ with signed weights $\mu_{t,\ell}^{(q)}$.

This factorization separates two complementary aspects of temporal credit assignment: (i) $\bar{m}_\mu(\ell)$ captures the average informational alignment between the gradient signal and the parameter-sensitivity directions at lag ℓ , and (ii) $f(\ell)$ quantifies the aggregate gain describing how much of that information survives recurrent transport through gates and state dynamics. Together, they determine the expected strength of the lagged contribution to the overall gradient, that is, how detectable past dependencies remain after being filtered by the network’s temporal mechanisms.

²Formally, $\mathbb{E}[\operatorname{sgn}(m_q(\ell)) \zeta_{t,\ell}^{(q)}] = |m_q(\ell)|$ by definition of $m_q(\ell)$. Thus the expected signal contained in $S_{t,\ell}$ is always nonnegative, irrespective of the sign pattern of the raw alignments $m_q(\ell)$. The sign $\operatorname{sgn}(m_q(\ell))$ should be understood as a population-level orientation defining an ideal matched statistic; in practice, detectability depends only on the magnitude of the mean shift and is assessed from the empirical average of $S_{t,\ell}$, without requiring prior knowledge of this sign.

Averaging $S_{t,\ell}$ over N independent training sequences yields $\widehat{S}_N(\ell) = \frac{1}{N} \sum_{n=1}^N S_{t,\ell}^{(n)}$, the empirical matched statistic that forms the basis for the finite-sample analysis in the next section.

5.3 Finite-sample analysis

We derive the finite-sample requirements for detecting a lag- ℓ dependency from noisy gradient information.

5.3.1 Statistical model

Empirical studies of SGD indicate that gradient fluctuations in deep networks are well described by a SaS distribution with $1 \leq \alpha \leq 2$ rather than a Gaussian one [7, 45]. SaS random variables form a family of heavy-tailed laws indexed by the tail index $\alpha \in (0, 2]$. They are characterized by the characteristic function $\phi_X(t) = \exp(-\sigma^\alpha |t|^\alpha)$, where $\sigma > 0$ is a scale parameter controlling dispersion. Their probability densities generally lack closed form except in special cases (Gaussian for $\alpha=2$, Cauchy for $\alpha=1$, Lévy for $\alpha=1/2$) and decay with power-law tails as $p(x) \sim |x|^{-(1+\alpha)}$. For $\alpha < 2$, these distributions have infinite variance; moreover, the first moment is finite only when $\alpha > 1$ (it is undefined at $\alpha = 1$).

We extend the zero-mean formulation of [45] to a two-parameter location family, allowing small shifts in the mean corresponding to the presence or absence of a detectable signal. At lag ℓ , the averaged matched statistic $\widehat{S}_N(\ell)$ over N independent training sequences is modeled as

$$\widehat{S}_N(\ell) | B \sim \mathcal{S}\alpha\mathcal{S}\left(\theta_{\text{out}}, \sigma_\alpha(\ell)/N^{1-1/\alpha}\right), \quad \theta_{\text{out}} \in \left\{+\frac{1}{2}\Delta(\ell), -\frac{1}{2}\Delta(\ell)\right\}, \quad (33)$$

where θ_{out} is the location parameter, the mean separation $\Delta(\ell) = \overline{m}_\mu(\ell)f(\ell)$ quantifies the strength of the lag- ℓ signal, $\sigma_\alpha(\ell)$ acts as a noise-scale proxy, and $B \in \{0, 1\}$ describes the non-detection/detection outcome.

For analytical tractability, we assume bounded alignment and noise scales, $c_m \leq m_\mu(\ell) \leq C_m$ and $c_\sigma \leq \sigma_\alpha(\ell) \leq C_\sigma$, which guarantee well-defined sample-complexity constants without affecting the asymptotic exponents. The factor $N^{1-1/\alpha}$ encodes the slow concentration typical of α -stable averages, and a justification for this choice is discussed in Appendix C.

5.3.2 Information-theoretic bounds

The learnability problem at lag ℓ is equivalent to distinguishing between two SaS distributions with opposite location shifts, corresponding to the presence or absence of a detectable signal in the averaged matched statistic:

$$P_{\text{det}} = \mathcal{S}\alpha\mathcal{S}\left(+\frac{1}{2}\Delta(\ell), \sigma_\alpha(\ell)/N^{1-1/\alpha}\right), \quad P_{\text{non}} = \mathcal{S}\alpha\mathcal{S}\left(-\frac{1}{2}\Delta(\ell), \sigma_\alpha(\ell)/N^{1-1/\alpha}\right),$$

where $\Delta(\ell) = \overline{m}_\mu(\ell)f(\ell)$ denotes the mean separation.

For $\alpha > 1$, symmetric α -stable location families satisfy local asymptotic normality (LAN) under suitable normalization, enabling the use of information-theoretic bounds [21, 30, 38]. In the present setting, the empirical statistic $\widehat{S}_N(\ell)$ defines a triangular array of location models [48] whose scale shrinks with the number of sequences as $s_N = \sigma_\alpha(\ell)N^{1/\alpha-1}$. For such families, LAN holds with normalization rate $r_N = 1/s_N$, which governs the detectability thresholds derived below. As a consequence, the log-likelihood ratio between P_{det} and P_{non} admits a quadratic expansion for small location shifts, yielding the lower bound for the Kullback-Leibler (KL) divergence

$$D_{\text{KL}}(P_{\text{det}}\|P_{\text{non}}) \geq c_\alpha \frac{N^{2(1-1/\alpha)} \Delta(\ell)^2}{\sigma_\alpha(\ell)^2}, \quad (34)$$

where $c_\alpha > 0$ depends only on α . A derivation of this bound for shrinking-scale α -stable location models is provided in Appendix D.

Combining (34) with standard relations between KL divergence and mutual information [11] yields

$$I(B; \widehat{S}_N(\ell)) \geq \min \left\{ \log 2, c_\alpha \frac{N^{2(1-1/\alpha)}}{\sigma_\alpha(\ell)^2} \overline{m}_\mu(\ell)^2 f(\ell)^2 \right\}. \quad (35)$$

Applying Fano's inequality [11] to the binary detection problem yields the minimal number of independent sequences N required to achieve a target error probability $P_e \leq \epsilon$:

$$N \geq \left(\frac{\sigma_\alpha(\ell)}{\sqrt{c_\alpha} \overline{m}_\mu(\ell) f(\ell)} \right)^{\frac{\alpha}{\alpha-1}} \left(\log \frac{1}{2\epsilon} \right)^{\frac{\alpha}{2(\alpha-1)}}. \quad (36)$$

This expression links sample complexity to the noise scale $\sigma_\alpha(\ell)$, the average alignment $\overline{m}_\mu(\ell)$, and the envelope $f(\ell)$. In contrast to the Gaussian case, the exponent $\alpha/(\alpha-1) > 2$ for $\alpha < 2$, reflecting the slower statistical concentration induced by heavy-tailed gradient noise. Full derivations of Eqs. (35) and (36) are given in Appendix E.

5.4 Learnability window and scaling laws

Throughout this section we adopt the corrected concentration exponent

$$\kappa_\alpha := \frac{\alpha}{\alpha-1}, \quad \alpha > 1, \quad (37)$$

which governs the finite-sample detectability of lagged dependencies under α -stable gradient noise when statistics are averaged over independent sequences. Equivalently, the noise floor of the empirical matched statistic decays as $N^{-1/\kappa_\alpha} = N^{-(1-1/\alpha)}$.

Starting from the finite-sample condition in Eq. (36), we can invert the relation to express the minimal effective learning rate mass required for reliable detection at a given sample size N . Rearranging terms³ yields the per-lag detectability threshold

$$\varepsilon_{\text{th}}(\ell) = \frac{\sigma_\alpha(\ell)}{N^{1/\kappa_\alpha} \overline{m}_\mu(\ell)} \cdot \frac{1}{\sqrt{c_\alpha}} \sqrt{\log \left(\frac{1}{2\epsilon} \right)}. \quad (38)$$

This threshold compactly summarizes the interplay of noise scale $\sigma_\alpha(\ell)$, data size N , and alignment strength $\overline{m}_\mu(\ell)$: for a dependency at lag ℓ to be statistically detectable under heavy-tailed α -stable noise, the envelope $f(\ell)$ must exceed $\varepsilon_{\text{th}}(\ell)$. In this formulation, smaller α values (heavier tails) increase κ_α , thereby slowing statistical concentration to N^{1/κ_α} and reducing the effective temporal range over which informative gradients can be recovered.

We can now define the learnability window.

Definition 5.1 (Learnability window under α -stable noise). The *learnability window* is

$$\mathcal{H}_N = \sup \{ \ell \geq 1 : f(\ell) \geq \varepsilon_{\text{th}}(\ell) \}. \quad (39)$$

Intuitively, \mathcal{H}_N is the largest lag for which the transported gradient retains a recoverable signal. Even if Jacobians are numerically stable, once $f(\ell)$ falls below $\varepsilon_{\text{th}}(\ell)$, heavy-tailed fluctuations dominate and credit assignment becomes statistically infeasible.

From the Fano bound in Eq. (36), the minimal number of independent sequences sufficient to detect a lag- ℓ dependency can be written as

$$N(\ell) := \kappa_{\alpha,\epsilon} \left(\frac{\sigma_\alpha(\ell)}{\overline{m}_\mu(\ell) f(\ell)} \right)^{\kappa_\alpha}, \quad \kappa_{\alpha,\epsilon} := \frac{1}{c_\alpha^{\kappa_\alpha/2}} \left(\log \frac{1}{2\epsilon} \right)^{\kappa_\alpha/2}. \quad (40)$$

The factor $\kappa_{\alpha,\epsilon}$ depends only on the tail index α and the target error level ϵ (fixed across lags) and will be absorbed into constant factors in our asymptotic statements.

Here, we formalize two regularities that drive the scaling of \mathcal{H}_N . Proofs appear in Appendix F.

³To obtain Eq. (38) from Eq. (36), one takes the κ_α th root of the bound, isolates the factor $1/f(\ell)$, and inverts the (positive) inequality. This yields the minimal effective learning rate mass required for detectability at lag ℓ .

Lemma 5.1 (Monotonicity in the lag). Fix t and a neuron q . Assume gate activations lie in $[0, 1]$ and activation derivatives are bounded in $[0, 1]$. Then $\ell \mapsto |\mu_{t,\ell}^{(q)}|$ is nonincreasing and, consequently, $\ell_1 \leq \ell_2 \Rightarrow f(\ell_2) \leq f(\ell_1)$.

Lemma 5.2 (Sample-complexity scaling and window bounds). Assume there exist constants $0 < c_\sigma \leq C_\sigma$ and $0 < c_m \leq C_m$ such that, over the lags of interest, $c_\sigma \leq \sigma_\alpha(\ell) \leq C_\sigma$ and $c_m \leq \overline{m}_\mu(\ell) \leq C_m$. Then, with $N(\ell)$ defined in Eq. (40), there are constants $0 < c_\star \leq C_\star$ for which

$$c_\star f(\ell)^{-\kappa_\alpha} \leq N(\ell) \leq C_\star f(\ell)^{-\kappa_\alpha}, \quad c_\star := \kappa_{\alpha,\epsilon} \left(\frac{c_\sigma}{C_m} \right)^{\kappa_\alpha}, \quad C_\star := \kappa_{\alpha,\epsilon} \left(\frac{C_\sigma}{c_m} \right)^{\kappa_\alpha}. \quad (41)$$

Consequently, with $f^\leftarrow(y) = \sup\{\ell \geq 1 : f(\ell) \geq y\}$ being the generalized inverse of $f(\ell)$,

$$f^\leftarrow\left(\frac{C_\sigma}{c_m} N^{-1/\kappa_\alpha}\right) \leq \mathcal{H}_N \leq f^\leftarrow\left(\frac{c_\sigma}{C_m} N^{-1/\kappa_\alpha}\right). \quad (42)$$

The first lemma captures the monotone, multiplicative attenuation induced by gates; the second makes explicit that the per-lag sample complexity grows as the inverse κ_α -power of the envelope $f(\ell)$. Together, they reduce the problem of characterizing \mathcal{H}_N to inverting the decay profile of $f(\ell)$ at the level N^{-1/κ_α} . In other words, once $\sigma_\alpha(\ell)$ and $\overline{m}_\mu(\ell)$ are bounded, the temporal reach of learnability is controlled by the speed with which $f(\ell)$ decays with ℓ and by the heavy-tailed concentration exponent κ_α .

Canonical envelope scaling regimes. In practice, gated RNNs may exhibit intricate envelope profiles, including mixtures of decay regimes or multi-phase behavior across different lag ranges. To develop analytic insight, we focus on three canonical asymptotic scaling profiles that arise naturally from gate-induced multiplicative dynamics: logarithmic, polynomial, and exponential decay. These regimes provide a structural classification of how $f(\ell)$ can attenuate in the large-lag limit and form the basis of the corresponding learnability scaling laws. Real networks need not follow a single regime uniformly across all lags; finite-dimensional implementations and bounded gates inevitably induce crossover behavior, typically resulting in exponential-like cutoffs at sufficiently large ℓ . More complex envelope shapes can nevertheless be analyzed within the same framework by decomposing them into these canonical asymptotic components.

For each of these canonical asymptotic regimes of $f(\ell)$, we obtain the corresponding large- ℓ scaling laws (up to multiplicative constants):

- (i) **Logarithmic decay:** if $f(\ell) \asymp c/\log(1+\ell)$, then $N(\ell) \asymp [\log(1+\ell)]^{\kappa_\alpha}$ and $\mathcal{H}_N \asymp \exp(\kappa N^{1/\kappa_\alpha}) - 1$.
- (ii) **Polynomial decay:** if $f(\ell) \asymp c\ell^{-\beta}$, then $N(\ell) \asymp \ell^{\kappa_\alpha\beta}$ and $\mathcal{H}_N \asymp N^{1/(\kappa_\alpha\beta)}$.
- (iii) **Exponential decay:** if $f(\ell) \asymp c\lambda^\ell$ with $\lambda \in (0, 1)$, then $N(\ell) \asymp \lambda^{-\kappa_\alpha\ell}$ and $\mathcal{H}_N \asymp (\log N)/[\kappa_\alpha \log(1/\lambda)]$.

In these expressions, the symbol \asymp denotes equality at the level of asymptotic order. These scaling laws characterize how gating geometry and heavy-tailed noise jointly determine the large-lag behavior of temporal learnability. Exponential decay corresponds to rapid forgetting and only logarithmic growth of the horizon; polynomial decay yields algebraic horizon growth; and logarithmic decay represents a boundary regime with rapidly expanding \mathcal{H}_N . In all cases, smaller α compresses \mathcal{H}_N by increasing κ_α and slowing statistical concentration. Full derivations and constant factors are provided in Appendix G.

5.5 Theoretical implications

Combining the Fano-derived sample-complexity bound in Eq. (36) with the learnability window analysis of Sec. 5.4 yields several theoretical insights into how gating structure, noise statistics, and finite data interact to determine temporal learnability.

(i) Gate-controlled envelopes set sample complexity under heavy-tailed noise. The detectability of a lag- ℓ dependency is governed by the signal amplitude $\Delta(\ell) = \overline{m}_\mu(\ell) f(\ell)$, which grows linearly with the envelope $f(\ell)$ (see Eq. (31)). In the mutual information bound of Eq. (35), this signal enters quadratically as $\Delta(\ell)^2$, while the contribution of data enters through the concentration factor $N^{2(1-1/\alpha)} = N^{2/\kappa_\alpha}$.

When $\alpha < 2$, the dependence on N is sublinear, reflecting the slow statistical concentration of heavy-tailed averages. As a result, at fixed lag ℓ and up to bounded prefactors associated with $\overline{m}_\mu(\ell)$ and $\sigma_\alpha(\ell)$, increasing the envelope $f(\ell)$ through gating geometry yields a multiplicative gain in signal strength that dominates the effect of increasing the dataset size. This imbalance is made explicit by the Fano bound (36), which yields the *master proportionality*

$$N(\ell) \propto f(\ell)^{-\kappa_\alpha}. \quad (43)$$

Equation (43) identifies the envelope $f(\ell)$ as the primary control variable governing sample complexity under heavy-tailed noise. Importantly, it is a proportionality relation rather than a closed-form equality: it does not determine the dependence of $N(\ell)$ on ℓ by itself, but constrains how changes in sample complexity must track changes in the envelope.

Concrete scaling laws follow once this proportionality is combined with a specific decay regime for $f(\ell)$. For example, polynomial envelope decay yields algebraic growth of $N(\ell)$ and expanding learnability windows, whereas exponential decay leads to rapidly increasing sample requirements and finite horizons. Thus, under heavy-tailed statistics, the role of gating is not merely to stabilize gradients, but to shape the envelope $f(\ell)$ that determines the scaling class of temporal learnability.

(ii) The tail index α governs statistical efficiency. The concentration exponent $\kappa_\alpha = \alpha/(\alpha - 1)$ quantifies how rapidly noise averages out when statistics are aggregated across independent sequences. For Gaussian fluctuations ($\alpha = 2$), one recovers the familiar concentration rate $N^{-1/2}$; for $\alpha < 2$, the slower rate $N^{-1/\kappa_\alpha} = N^{-(1-1/\alpha)}$ substantially weakens the effective signal-to-noise ratio. Thus, even for identical gating geometry and identical envelopes $f(\ell)$, smaller values of α increase κ_α , compress the learnability window, and raise the number of samples required for reliable detection.

Importantly, this dependence implies that the effective scaling regime is determined jointly by the envelope $f(\ell)$ and the noise statistics, rather than by architectural structure alone.

(iii) Architectural and training implications. Architectures that permit slowly decaying envelopes are intrinsically capable of supporting long-range learnability under heavy-tailed noise. At the same time, such behavior is not guaranteed by architecture alone: training dynamics and noise statistics determine which decay regime is effectively realized. Conversely, training methods that reduce the impact of heavy-tailed fluctuations, such as clipping, normalization, or stabilizing adaptive optimizers, effectively increase α , thereby reducing κ_α and improving statistical efficiency without altering model capacity.

(iv) Vanishing learnability as an information-theoretic obstruction. The learnability window \mathcal{H}_N may vanish identically for certain architectures, meaning that $\mathcal{H}_N = 0$ for all finite N . In this case, the envelope $f(\ell)$ falls below the statistical detectability threshold for every $\ell \geq 1$, and the corresponding sample complexity $N(\ell)$ diverges. This does not reflect an optimization failure or insufficient data, but an *information-theoretic obstruction*: the transported gradients carry no statistically usable signal at nonzero lags. Equivalently, the KL divergence between the detection and non-detection models vanishes, so no estimator can reliably distinguish the two hypotheses regardless of sample size.

6 Empirical validation

The purpose of this section is not to compare architectures in terms of predictive performance, but to empirically probe how envelope decay, noise statistics, and gating structure interact to determine finite-horizon learnability. Here, learnability refers to the statistical detectability of gradient signal across lags, which is a necessary but not sufficient condition for successful task performance: if signal is not statistically

detectable, no consistent learning of long-range dependencies can occur, but detectability alone does not guarantee high predictive accuracy.

In particular, we aim to: (i) verify the monotone decay and scaling properties of the envelope $f(\ell)$ predicted by the analysis; (ii) quantify how the resulting empirical learnability windows $\hat{\mathcal{H}}_N$ depend on gating structure and sample size; and (iii) examine how the neuronwise time-scale spectra $\{\tau_q\}_q$ and the estimated gradient-noise statistics jointly correlate with the observed learnability regimes.

6.1 Experimental setup

Task and data. We consider a synthetic regression task defined on input–output pairs $\{(x_t, y_t)\}_{t=1}^T$, where $x_t \in \mathbb{R}^{16}$ and the target $y_t \in \mathbb{R}$ is scalar. All experiments use sequences of length $T = 1024$.

The target is generated as a weighted sum of delayed inputs,

$$y_t = \sum_{k=1}^5 c_k u^\top x_{t-\ell_k} + \varepsilon_t, \quad (44)$$

where $u \in \mathbb{R}^{16}$ is a random unit vector, the task lags are $\{\ell_k\} = \{32, 64, 128, 192, 256\}$, the mixing coefficients are $\{c_k\} = \{0.6, 0.5, 0.4, 0.32, 0.26\}$, and ε_t is independent Gaussian noise with standard deviation $\sigma_{\text{noise}} = 0.3$. These delayed components induce informative dependencies spanning short, intermediate, and relatively long temporal scales.

Each model is trained on 8000 independent sequences. All effective learning-rate and envelope statistics are computed on an independent diagnostic set of 8000 fresh sequences generated from the same data-generating process. No sequences are reused across training and diagnostic splits.

To assess temporal credit assignment independently of the specific task lags, all diagnostic quantities are evaluated on a separate lag grid $\ell \in [4, 256]$ consisting of 128 uniformly spaced values. This grid covers both sub-task and supra-task temporal scales, allowing us to probe the full decay profile of the learned envelope.

Architectures. We consider five recurrent architectures spanning increasing gating expressivity and time-scale heterogeneity: ConstGate, SharedGate, DiagGate, GRU, and LSTM.

The first three models share a common backbone update of the form

$$h_t = (1 - s_t) \odot h_{t-1} + s_t \odot \tilde{h}_t, \quad \tilde{h}_t = \tanh(W_h x_t + U_h h_{t-1} + b_h),$$

with hidden state $h_t \in \mathbb{R}^H$. The gate variable s_t controls the effective time scale of each unit. The architectures differ in the structure of this gate: (i) ConstGate uses a fixed scalar gate $s \in (0, 1)$ shared across all units and time steps; (ii) SharedGate uses a learned scalar gate $s_t \in (0, 1)$ shared across units and varying in time; and (iii) DiagGate uses a learned per-neuron gate $s_t \in (0, 1)^H$, updated coordinatewise from the current input and previous hidden state.

In addition, we include standard GRU and LSTM architectures, which implement multi-gate mechanisms and internal memory dynamics. These models realize richer mixtures of time scales through their reset/update (GRU) and input/forget/output (LSTM) gating structures.

All models use hidden dimension $H = 128$ and a linear readout $y_t = w^\top h_t$ trained with mean-squared error loss. Recurrent weight matrices are initialized orthogonally, biases are initialized to zero unless otherwise stated, and gate pre-activations in learned-gate models are initialized near zero, yielding initial gate values close to $\frac{1}{2}$ and well-conditioned initial time scales, consistent with the time-scale initialization heuristic of [33].

For brevity in figures and legends, we denote ConstGate, SharedGate, DiagGate, LSTM, and GRU by *const*, *shared*, *diag*, *lstm*, and *gru*, respectively. These abbreviated labels are used solely for visualization purposes.

Training protocol. All models are trained using mini-batch AdamW [34] with base learning rate $\mu = 10^{-3}$, weight decay $\lambda = 10^{-4}$, batch size $B = 512$, and gradient clipping at ℓ_2 norm 1.0. Training uses 8000 independent sequences of length $T = 1024$ for 500 epochs. No learning-rate schedule is applied, and all architectures share identical optimization hyperparameters.

After training, parameters are frozen and all diagnostics are computed on an independent set of 8000 fresh sequences generated from the same data-generating process, with no overlap in sequences or random seeds. All reported envelope, effective learning-rate, and noise statistics are evaluated under these frozen post-training parameters.

In the main text we employ AdamW, which can be interpreted as SGD with decoupled weight decay and adaptive preconditioning. Adaptive optimizers such as Adam and AdamW are known to preserve heavy-tailed gradient fluctuations even in the presence of gradient clipping, while providing improved numerical conditioning in practice [7]. We verified that disabling gradient clipping yields qualitatively similar envelope and noise statistics (results not shown), indicating that clipping affects numerical stability but not the scaling regimes of interest.

To clarify the role of the optimizer in shaping effective time-scale geometry, additional experiments with plain SGD and SGD with momentum are reported in Appendix H.

Effective learning rates. For each trained model, we estimate the effective learning rates $\mu_{t,\ell}^{(q)}$ derived in the state-parameter coupling analysis, evaluated under frozen post-training parameters. For GRU and LSTM, effective learning rates are computed using the definitions introduced in Section 4; for the diagonally gated models (ConstGate, SharedGate, DiagGate), we use the corresponding definitions provided in Appendix B.

For every diagnostic lag ℓ and unit q , the magnitudes $|\mu_{t,\ell}^{(q)}|$ are computed across the diagnostic set and averaged over time and independent sequences. The empirical envelope is then defined as

$$\hat{f}(\ell) = \sum_q \langle |\mu_{t,\ell}^{(q)}| \rangle,$$

corresponding to an ℓ_1 aggregation of neuronwise effective learning rates at lag ℓ .

Heavy-tailed statistics and empirical learnability window. For each diagnostic lag ℓ , we compute the empirical matched statistic introduced in Sec. 5.2 on the diagnostic set. From these statistics, we estimate the parameters of an α -stable law using McCulloch’s quantile-based estimator [37], obtaining a lag-dependent tail index $\hat{\alpha}(\ell)$ and scale parameter $\hat{\sigma}_\alpha(\ell)$. Although $\hat{\alpha}(\ell)$ is estimated separately for each lag, it concentrates around a model-dependent value with only mild lag-to-lag fluctuations. We therefore interpret the gradient noise as belonging to an approximately stable class characterized by an effective tail index $\hat{\alpha}$, while retaining the full lag dependence of the noise scale $\hat{\sigma}_\alpha(\ell)$.

These empirical noise estimates are combined with the measured envelope $\hat{f}(\ell)$ to evaluate the detectability condition derived in Sec. 5. For a given training budget N , we define the empirical learnability window as

$$\hat{\mathcal{H}}_N = \max \left\{ \ell : \hat{f}(\ell) \geq \varepsilon_{\text{th}}^{\text{emp}}(\ell; N) \right\}, \quad (45)$$

where $\varepsilon_{\text{th}}^{\text{emp}}(\ell; N)$ denotes the empirical detectability threshold obtained by substituting $\hat{\alpha}$ and $\hat{\sigma}_\alpha(\ell)$ into the theoretical criterion. This construction mirrors the definition of the theoretical learnability horizon \mathcal{H}_N , while avoiding explicit inversion of the sample-complexity relation.

Time-scale extraction. To characterize the temporal structure induced by each architecture, we extract a characteristic time scale for every neuron by fitting an exponential model

$$|\mu_{t,\ell}^{(q)}| \approx C_q \exp(-\ell/\tau_q)$$

to the neuronwise effective learning rates measured on the diagnostic set. The fitted parameter τ_q provides a dominant decay constant for unit q , interpreted as its effective time scale.

We summarize the resulting temporal organization through the empirical distribution $\{\tau_q\}_q$ across units. In addition, we report an aggregate envelope time scale τ_{env} obtained from an exponential fit to the macroscopic envelope $\hat{f}(\ell)$. While some architectures exhibit nearly single-scale exponential decay, others display broader mixtures of time scales; in those cases, the fitted τ_q values capture the leading local decay mode of each unit.

6.2 Results

Envelope scaling. Figure 1 (left) shows the estimated envelopes $\hat{f}(\ell)$ for ConstGate, SharedGate, DiagGate, GRU, and LSTM. All architectures exhibit monotone decay with increasing lag, but with markedly different attenuation regimes.

ConstGate and SharedGate display rapid envelope decay. On a semi-logarithmic scale (middle), both curves are well approximated by straight lines, consistent with exponential attenuation. Exponential fits of the form $\hat{f}(\ell) \approx c \exp(-\lambda\ell)$ yield decay rates $\lambda_{\text{const}} \approx 0.68$ and $\lambda_{\text{shared}} \approx 0.39$, with coefficients of determination $r^2 \approx 0.99$ and $r^2 \approx 0.99$, respectively. Power-law fits perform substantially worse ($r^2 \approx 0.86$ and $r^2 \approx 0.85$), confirming that these architectures lie firmly in the exponential regime. Their envelopes decay by several orders of magnitude within a few tens of lags, indicating a short effective temporal range.

DiagGate exhibits qualitatively slower attenuation. An exponential fit yields a small decay rate $\lambda_{\text{diag}} \approx 0.020$ ($r^2 \approx 0.99$), corresponding to a very long effective time scale. However, on a log-log scale (right), the envelope displays an approximately linear trend over the diagnostic range. A power-law fit $\hat{f}(\ell) \approx c\ell^{-\beta}$ yields $\beta_{\text{diag}} \approx 1.71$ with $r^2 \approx 0.93$. The exponential and algebraic models therefore provide comparable descriptions over the finite lag window explored in our experiments. In DiagGate, the exponential fit is characterized by an extremely small decay rate, so that over the observed range of lags the curve is nearly indistinguishable from a power-law trend. We therefore interpret DiagGate as operating in an intermediate regime: empirically consistent with approximate polynomial scaling across the explored window, yet theoretically compatible with an eventual exponential cut-off at sufficiently large lags.

GRU and LSTM extend this heterogeneous behavior. For GRU, exponential and power-law fits achieve comparable goodness of fit ($\lambda_{\text{gru}} \approx 0.018$, $r^2 \approx 0.97$; $\beta_{\text{gru}} \approx 1.59$, $r^2 \approx 0.96$), indicating a very slow exponential attenuation. Over the finite lag window explored, this shallow exponential is empirically difficult to distinguish from a power-law trend, although the two imply different asymptotic scaling regimes. For LSTM, the distinction is sharper: the exponential fit is comparatively weaker ($\lambda_{\text{lstm}} \approx 0.011$, $r^2 \approx 0.91$), whereas the power-law fit yields $\beta_{\text{lstm}} \approx 1.01$ with $r^2 \approx 0.99$. Over the diagnostic range, the LSTM envelope therefore aligns closely with polynomial scaling, with an exponential cut-off necessarily emerging at sufficiently large lags due to finite-state dynamics.

The interpretation of an intermediate algebraic-like regime for DiagGate, GRU, and LSTM is further supported by the decay of the complementary cumulative distribution function (CCDF) of the neuronwise effective time scales, reported below. In these architectures, the tail of the CCDF exhibits a slow decay compatible with a broad distribution of time constants, followed by a clear attenuation at large scales. This pattern is consistent with an approximate power-law-like behavior over intermediate lags, combined with an inevitable exponential cut-off induced by finite-dimensional state dynamics.

Collectively, these results reveal a hierarchy of temporal regimes: homogeneous scalar gating produces fast exponential decay; diagonal gating induces slow, approximately algebraic attenuation; and multi-gate architectures such as GRU and LSTM realize broad mixtures of time scales that manifest as approximate power-law scaling over intermediate horizons. Importantly, the corresponding state Jacobians remain numerically well-conditioned in all cases (results not shown), indicating that Jacobian stability alone does not determine finite-horizon learnability. Rather, it is the geometry of the envelope that governs the persistence of gradient signal across lags. All models exhibit consistent training loss reduction and stable optimization trajectories (learning curves not shown), confirming that they successfully fit the task under the shared training protocol. However, the objective of this study is not to fine-tune architectures for maximal predictive accuracy, but to characterize the structural conditions under which long-range dependencies remain statistically detectable.

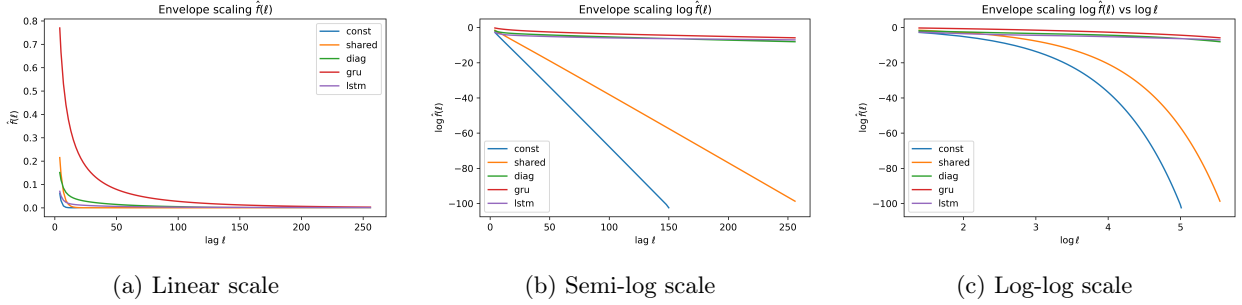


Figure 1: Envelopes of the effective learning rates $\hat{f}(\ell)$ for ConstGate, SharedGate, DiagGate, GRU, and LSTM models. **(a)** Linear scale. **(b)** Semi-logarithmic representation highlights the rapid exponential decay of ConstGate and SharedGate and the much slower attenuation of DiagGate, GRU, and LSTM. **(c)** Log-log representation reveals approximate polynomial scaling over intermediate lags for DiagGate, GRU, and LSTM, with an eventual exponential cut-off implied by finite-state dynamics.

Empirical learnability windows. From the measured envelopes $\hat{f}(\ell)$ and the estimated heavy-tailed noise parameters, we evaluate the empirical detectability condition for varying training budgets N and construct the corresponding learnability window $\hat{\mathcal{H}}_N$ defined in Eq. (45). Figure 2 reports $\hat{\mathcal{H}}_N$ as a function of the number of independent training sequences.

ConstGate and SharedGate exhibit short but finite learnability horizons that remain essentially constant as N increases. For ConstGate, the window saturates at small lags ($\hat{\mathcal{H}}_N \approx 30$), while SharedGate reaches a larger but still bounded plateau ($\hat{\mathcal{H}}_N \approx 65\text{--}70$). Increasing the training budget produces only marginal extensions. This behavior is consistent with the exponential envelope regime: when $\hat{f}(\ell)$ decays exponentially, the detectability threshold grows rapidly with lag, so that over practical sample sizes the horizon appears effectively independent of N .

DiagGate displays qualitatively different behavior. For small N , the learnability window is negligible. Once the budget exceeds a few hundred sequences, $\hat{\mathcal{H}}_N$ expands in discrete steps, progressively reaching intermediate and longer lags and stabilizing near $\hat{\mathcal{H}}_N \approx 120$ for the largest budgets considered. This data-dependent expansion is consistent with the observed approximately algebraic envelope regime: slow attenuation allows additional lags to cross the detectability threshold as N increases.

GRU and LSTM exhibit an even more pronounced extension of the horizon. Both architectures display a sharp transition: below a critical sample size the horizon is effectively zero, whereas above this threshold the window rapidly expands to the maximal diagnostic lag ($\hat{\mathcal{H}}_N \approx 256$). This behavior reflects their broad mixture of time scales and slow envelope decay over intermediate lags. In these models, once the training budget exceeds the noise-dominated regime, a large portion of the temporal range becomes detectable within the explored horizon.

Taken together, these results confirm the structural prediction of the theory: exponential envelope decay leads to early saturation of the learnability window, whereas slow, approximately algebraic attenuation enables systematic expansion of the horizon with increasing data. These behaviors are precisely those implied by the master proportionality $N(\ell) \propto f(\ell)^{-\kappa\alpha}$, which links envelope geometry to sample complexity under heavy-tailed noise.

Direct inversion of the detectability relation to estimate lag-dependent sample-complexity exponents is statistically unstable near the detectability boundary and highly sensitive to finite-sample fluctuations. Moreover, such inversion does not provide additional structural insight beyond what is already captured by the envelope decay regime and the resulting behavior of $\hat{\mathcal{H}}_N$. We therefore adopt the learnability window as the primary empirical observable, as it offers a robust and interpretable summary of the scaling consequences of the theory.

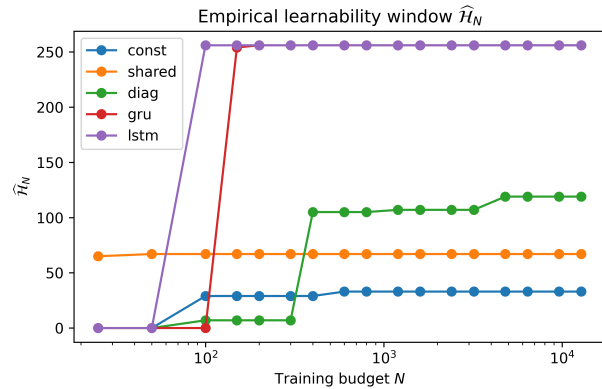


Figure 2: Empirical learnability windows \hat{H}_N for ConstGate, SharedGate, DiagGate, GRU, and LSTM. ConstGate and SharedGate (blue and orange) exhibit short but finite learnability horizons that remain essentially constant as the number of independent training sequences N increases, reflecting the rapid exponential decay of their envelopes $\hat{f}(\ell)$. DiagGate (green) displays a qualitatively different pattern: once N exceeds a few hundred sequences, the learnability window expands to intermediate and longer lags, stabilizing near $\hat{H}_N \approx 120$ for the largest budgets considered. GRU (red) and LSTM (purple) exhibit a sharp transition behavior: below a critical sample size the horizon is negligible, whereas above this threshold the window rapidly extends to the maximal diagnostic lag, consistent with their slow envelope attenuation and broad mixture of time scales.

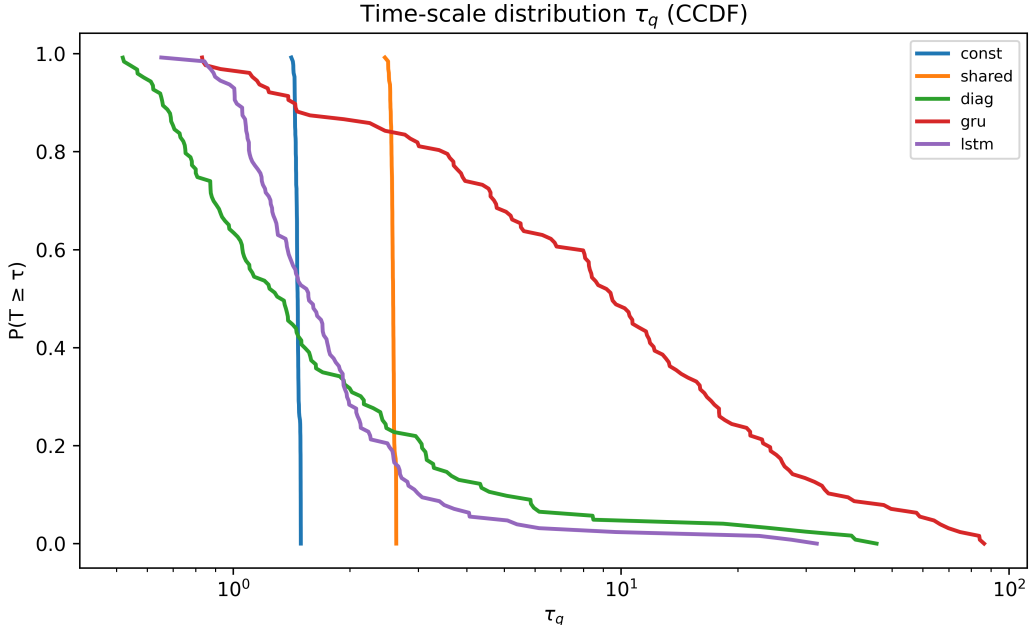


Figure 3: Complementary cumulative distribution functions (CCDFs) of the neuronwise effective time scales τ_q . ConstGate and SharedGate exhibit narrowly concentrated spectra, whereas DiagGate, GRU, and LSTM display broad heterogeneous distributions with a slowly decaying intermediate tail and a visible attenuation at large τ , consistent with a mixed multi-scale regime.

Time-scale spectra. To connect the envelope geometry back to gating, we inspect the distribution of neuronwise time scales $\{\tau_q\}_q$ inferred from the effective learning rates. Rather than relying solely on density estimates, we summarize these spectra via the CCDF, $\mathbb{P}(\tau_q \geq \tau)$, which directly quantifies the fraction of units operating on time scales longer than τ . Figure 3 reports the empirical CCDFs for all architectures on a log-scaled τ axis, which makes heterogeneity in the slow tail immediately visible.

ConstGate exhibits an essentially degenerate spectrum, with all units clustered around a single characteristic time scale. SharedGate displays a similarly narrow spectrum, with only minor unit-to-unit variability. In contrast, DiagGate produces a broad and heterogeneous time-scale distribution: most units operate on short time scales, while a non-negligible fraction populates intermediate ranges and a small subpopulation extends to substantially longer τ values. GRU and LSTM further accentuate this heterogeneity, exhibiting particularly slowly decaying CCDF tails over intermediate τ together with a clear attenuation at the largest time scales. This mixed pattern, slow tail decay over an intermediate range followed by an effective cut-off, is consistent with the envelope behavior reported above: architectures with broader spectra and a slow tail support substantially extended temporal transport over finite horizons, whereas narrowly concentrated spectra correlate with rapid exponential envelope decay and early saturation of $\widehat{\mathcal{H}}_N$. Additional tail-emphasis visualizations and per-model density diagnostics are reported in Appendix I, which further illustrate the heterogeneous multi-scale structure underlying these regimes.

Noise statistics and selection of scaling regimes. An additional empirical observation helps clarify why different architectures operate in distinct learnability regimes. Alongside differences in time-scale spectra, we observe systematic differences in the statistics of gradient noise across models. Figure 4 shows the empirical distributions of the lag-wise estimated tail index $\hat{\alpha}(\ell)$, while Fig. 5 reports the corresponding noise scale $\hat{\sigma}_\alpha(\ell)$ as a function of lag. The tail index primarily governs the rate of statistical concentration, whereas

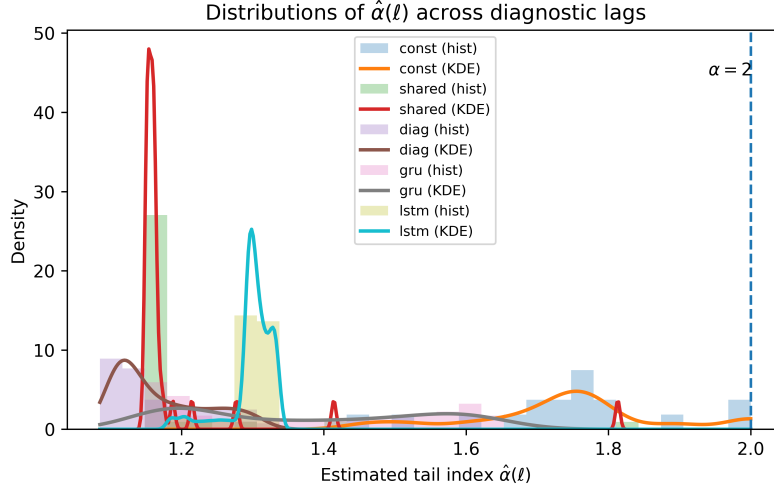


Figure 4: Empirical distributions of the lag-wise estimated gradient-noise tail index $\hat{\alpha}(\ell)$ across diagnostic lags for all architectures. ConstGate and SharedGate concentrate close to the Gaussian limit $\alpha = 2$, indicating relatively efficient statistical concentration of gradient fluctuations. In contrast, DiagGate, GRU, and LSTM exhibit systematically heavier-tailed behavior with $\hat{\alpha}(\ell) < 2$, corresponding to slower concentration of empirical averages. These differences in noise statistics align with the emergence of broader time-scale spectra, slower envelope attenuation, and extended learnability windows.

the scale $\hat{\sigma}_\alpha(\ell)$ sets the lag-dependent noise floor entering the detectability threshold.

ConstGate and SharedGate operate close to the Gaussian regime, with $\hat{\alpha}(\ell)$ concentrated near the upper stability limit $\alpha = 2$ across diagnostic lags. In these models, empirical averages concentrate rapidly, and the estimated noise scale $\hat{\sigma}_\alpha(\ell)$ decays sharply with lag, indicating that gradient fluctuations become negligible at moderate temporal distances. In this setting, the fast exponential decay of the envelope $f(\ell)$ remains compatible with the observed, short learnability horizons.

DiagGate exhibits systematically heavier-tailed fluctuations, with $\hat{\alpha}(\ell)$ concentrated strictly below 2, implying slower statistical concentration. Moreover, its noise scale $\hat{\sigma}_\alpha(\ell)$ decays much more slowly with lag, remaining non-negligible over the full diagnostic range. GRU and LSTM display similarly heavy-tailed behavior, with tail indices bounded away from 2 and persistent noise scales across lags. Under such noise statistics, rapidly decaying exponential envelopes incur a substantially higher statistical cost, as signal strength falls below the detectability threshold before empirical averages can concentrate. Consequently, regimes sustaining larger values of $f(\ell)$ over extended lags—via broader mixtures of time scales—become comparatively more viable under finite data.

Importantly, these results indicate that the realized scaling behavior is not determined by architecture alone. Rather, gating geometry defines the space of accessible time-scale spectra, while the interaction between training dynamics and emergent noise statistics selects which scaling regime is stabilized in practice.

7 Discussion and future directions

This work develops a quantitative framework linking gating geometry, heavy-tailed gradient noise, and the finite-horizon learnability of recurrent neural networks. A central message is that effective learning rates $\mu_{t,\ell}$, rather than Jacobian stability in isolation, determine how much gradient signal remains statistically

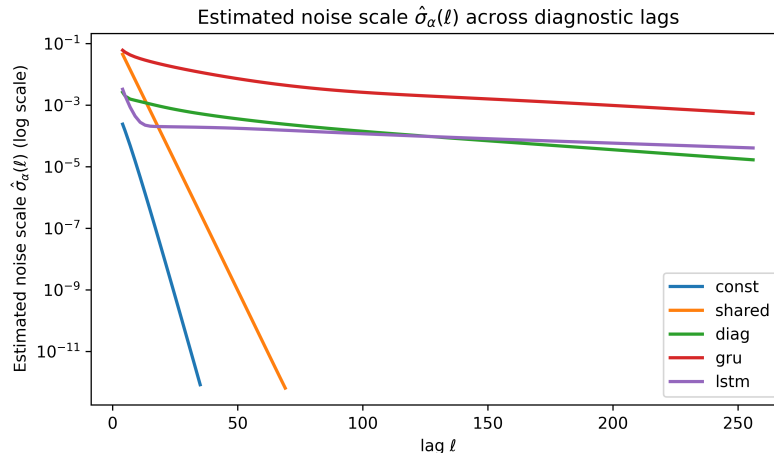


Figure 5: Estimated lag-dependent noise scale $\hat{\sigma}_\alpha(\ell)$ for all architectures (log scale). ConstGate and SharedGate exhibit rapidly decaying noise scales, indicating fast statistical concentration of gradient fluctuations. By contrast, DiagGate, GRU, and LSTM maintain substantially larger fluctuation levels across lags, with markedly slower decay. Such persistent noise at long temporal distances increases the statistical cost of rapidly vanishing envelopes and is consistent with the emergence of slower, more robust scaling regimes.

detectable across temporal lags. The decay profile of the envelope $f(\ell)$, together with the heavy-tailed index α through the concentration exponent $\kappa_\alpha = \alpha/(\alpha - 1)$, governs the detectability threshold and hence the learnability window \mathcal{H}_N .

Our empirical results support this theoretical picture while clarifying the role of architectural inductive bias. Architectures with constrained gating tend to induce narrow and nearly synchronized time-scale spectra, leading to fast exponential decay of the envelope and short, largely data-insensitive learnability windows. Architectures capable of neuronwise or multi-gate modulation admit heterogeneous mixtures of time scales and can realize slower attenuation regimes, within which the learnability window expands systematically with available data. The decisive factor is not nominal architectural complexity, but the dispersion of effective time scales that emerges during training.

The emergence of algebraic-like envelope behavior should be interpreted as a finite operational regime rather than as an asymptotic property. In finite-dimensional recurrent systems, true scale invariance over arbitrarily large lags is structurally impossible: hidden dimension, sequence length, numerical precision, and data budget are all finite. Even when a broad hierarchy of effective time scales induces an approximately polynomial decay of $f(\ell)$ over an extended intermediate range, finite-size effects ultimately impose a crossover once the effective signal strength falls below the detectability threshold. Polynomial scaling is therefore a windowed phenomenon whose extent is jointly determined by envelope geometry and noise statistics.

At the same time, the realized scaling regime is not deterministic. Even architectures with rich gating structure may converge to synchronized time scales and revert to the exponential regime, depending on training dynamics, optimization hyperparameters, and task statistics. Gating geometry defines the space of accessible time-scale spectra, but does not uniquely determine which regime is selected.

Within this classification, the logarithmic decay regime represents a formal boundary case. It corresponds to extremely slow attenuation of $f(\ell)$ and rapidly expanding learnability windows, and may be viewed as a critical configuration separating algebraic from exponential forgetting. We conjecture that such a regime cannot be stably maintained in finite recurrent networks without substantial fine tuning of the gate-induced time-scale spectrum. Finite-dimensional constraints and training dynamics are likely to destabilize this boundary configuration, leading either to collapse toward synchronized exponential decay or to relaxation

into heterogeneous but still algebraic mixtures of time scales. Understanding whether recurrent systems can approach this boundary regime, even transiently, remains an open theoretical question.

Empirically, we observe that the scaling regime realized by a trained model is systematically accompanied by distinct gradient-noise statistics. Architectures operating in slow-decay regimes exhibit heavier-tailed gradient noise and persistent noise scales across lags, whereas synchronized exponential regimes tend to operate closer to Gaussian concentration. Under heavy-tailed noise, rapid exponential decay of the envelope becomes statistically costly in finite data settings, as signal strength falls below the detectability threshold before empirical averages can concentrate. Heavy-tailed fluctuations therefore act as a viability constraint, disfavoring rapid forgetting and effectively selecting, among the dynamical regimes accessible to an architecture, those that preserve signal over longer temporal scales. This constraint does not dictate how training reaches such regimes, but delineates which regimes can persist as learnable solutions.

These observations highlight three broader implications. First, the temporal horizon of learnability is controlled by envelope geometry rather than by Jacobian stability alone. Second, gating architectures shape the space of attainable time-scale spectra, biasing—but not guaranteeing—the emergence of heterogeneous dynamics that support long-range credit assignment. Third, under heavy-tailed gradient noise, increasing the number of training sequences yields diminishing returns for architectures operating in the exponential regime, whereas modifying gating geometry can alter the scaling class of temporal learnability.

From an empirical standpoint, a natural next step is to conduct a broader experimental campaign exploring how different architectural variants, training objectives, optimization schemes, and task statistics influence the realized time-scale spectra and noise regimes. Systematic variation of hidden dimension, gating parametrizations, regularization strategies, and data complexity would help clarify which factors promote or suppress heterogeneous time-scale mixtures, and how robust the observed scaling classes are across problem settings.

More broadly, the framework introduced here is not tied to a specific architecture. It applies to learning systems trained with SGD-like optimizers whenever signals must propagate through long chains of Jacobians. We focused on gated recurrent networks because their dynamics admit a transparent interpretation in terms of tunable time scales, making the connection between temporal credit assignment, effective learning rates, and statistical detectability explicit. Similar limitations are expected in deep or sequence models where temporal depth can be traded for layer depth, suggesting that the notion of finite-horizon learnability extends beyond classical recurrent settings.

Finally, our results raise a deeper open question: why do some architectures spontaneously develop broad time-scale spectra during training, while others collapse to synchronized dynamics? The present framework establishes which scaling regimes are statistically viable under finite data and heavy-tailed noise by characterizing how envelope decay and noise statistics jointly constrain detectability. It does not, however, explain how training dynamics explore the space of accessible regimes or why particular configurations are selected. A complementary dynamical theory addressing the emergence or collapse of mixed time scales—potentially arising from the coupled evolution of states, gates, and parameters—would be an important step toward a unified understanding of long-range memory formation in trained deep learning systems.

A Matrix product expansion via the Fréchet derivative formulation

This section summarizes the first-order expansion of a product of matrices with structured perturbations introduced in [33].

Definition A.1 (Fréchet differentiability [18, 27]). Let $f : \mathbb{C}^{n \times n} \rightarrow \mathbb{C}^{n \times n}$. We say that f is *Fréchet differentiable* at $A \in \mathbb{C}^{n \times n}$ if there exists a bounded linear mapping $L_f(A, \cdot)$ such that

$$\lim_{\|E\| \rightarrow 0} \frac{\|f(A+E) - f(A) - L_f(A, E)\|}{\|E\|} = 0. \quad (46)$$

If f is Fréchet differentiable at A ,

$$f(A+E) = f(A) + L_f(A, E) + o(\|E\|). \quad (47)$$

If g and h are Fréchet differentiable at A and $f(X) = g(X)h(X)$, then

$$L_{gh}(A, E) = L_g(A, E)h(A) + g(A)L_h(A, E). \quad (48)$$

Consider

$$F(\varepsilon) = \prod_{j=1}^n (A_j + \varepsilon B_j), \quad (49)$$

with $A_j, B_j \in \mathbb{C}^{d \times d}$. By recursive application of (48) one obtains

$$L_{F_n}(0, E) = \sum_{i=1}^n \left(\prod_{j=1}^{i-1} A_j \right) B_i \left(\prod_{j=i+1}^n A_j \right), \quad (50)$$

and the first-order expansion

$$F(\varepsilon) = \left(\prod_{j=1}^n A_j \right) + \varepsilon \sum_{m=1}^n \left(\prod_{j=m+1}^n A_j \right) B_m \left(\prod_{j=1}^{m-1} A_j \right) + O(\varepsilon^2). \quad (51)$$

B Diagonally gated RNNs: One-step Jacobians and effective learning rates

We introduce diagonally gated RNN models previously considered in [33] that we use throughout the paper: a per-neuron (diagonal) gate, a shared (global) gate, and a constant gate. All follow the same update template:

$$h_t = (1 - s_t) \odot h_{t-1} + s_t \odot \tilde{h}_t, \quad \tilde{h}_t = \tanh(a_t^h), \quad a_t^h = W_h x_t + U_h h_{t-1} + b_h,$$

but differ in how the gate s_t is produced. We reuse the conventions of Sec. 4.

(a) Per-neuron (diagonal) gate $s_t \in (0, 1)^H$ (“DiagGate”)

The gate is computed per coordinate:

$$a_t^s = W_s x_t + U_s h_{t-1} + b_s, \quad s_t = \sigma(a_t^s) \in (0, 1)^H. \quad (52)$$

Define $S_t := D(s_t)$ and $S_t^s := S^\sigma(a_t^s)$. The exact one-step Jacobian $J_t = \partial h_t / \partial h_{t-1} \in \mathbb{R}^{H \times H}$ is

$$J_t = \underbrace{(I - S_t)}_{\text{leak}} + \underbrace{(D(\tilde{h}_t) - D(h_{t-1})) S_t^s U_s}_{\text{gate sensitivity}} + \underbrace{S_t S_t^h U_h}_{\text{candidate path}}. \quad (53)$$

Here the leak term $(I - S_t)$ is diagonal; the remaining two terms contain U_s and U_h and are generally full rank, mixing information across neurons.

Effective learning rates. The zeroth-order envelope is given by

$$\gamma_{t,\ell}^{(0,q)} = \prod_{j=\ell+1}^t (1 - s_{j,q}),$$

yielding per-neuron effective learning rates

$$\mu_{t,\ell}^{(q)} = \mu \left(\gamma_{t,\ell}^{(0,q)} + \gamma_{t,\ell}^{(1,q)} \right),$$

where $\gamma_{t,\ell}^{(1,q)}$ arises from the diagonal of the gate-sensitivity and candidate-path corrections in Eq. (53).

(b) Shared (global) scalar gate $s_t \in (0, 1)$ (“SharedGate”)

The gate is a single scalar per time step (and per sequence element in a batch):

$$a_t^s = w_s^\top x_t + u_s^\top h_{t-1} + b_s, \quad s_t = \sigma(a_t^s) \in (0, 1). \quad (54)$$

The update is $h_t = (1 - s_t)h_{t-1} + s_t\tilde{h}_t$ with $\tilde{h}_t = \tanh(a_t^h)$. Using $\partial s_t / \partial h_{t-1} = s_t(1 - s_t)u_s$, the Jacobian is

$$J_t = \underbrace{(1 - s_t)I}_{\text{leak}} + \underbrace{s_t S_t^h U_h}_{\text{candidate path}} + \underbrace{s_t(1 - s_t)(\tilde{h}_t - h_{t-1})u_s^\top}_{\text{rank-1 gate sensitivity}}. \quad (55)$$

The last term is a rank-1 outer product and is the only source of cross-neuron coupling other than U_h .

Effective learning rates. The zeroth-order envelope is

$$\gamma_{t,\ell}^{(0)} = \prod_{j=\ell+1}^t (1 - s_j),$$

which is identical for all neurons. Hence

$$\mu_{t,\ell}^{(q)} = \mu \left(\gamma_{t,\ell}^{(0)} + \gamma_{t,\ell}^{(1,q)} \right),$$

with neuron-dependent corrections $\gamma_{t,\ell}^{(1,q)}$ coming from the rank-1 gate sensitivity and candidate path in Eq. (55).

(c) Constant scalar gate $s \in (0, 1)$ (“ConstGate”)

As a minimal baseline we fix the gate value to a constant scalar $s \in (0, 1)$, independent of t , inputs, or hidden state. The update is

$$h_t = (1 - s)h_{t-1} + s\tilde{h}_t, \quad \tilde{h}_t = \tanh(a_t^h), \quad a_t^h = W_h x_t + U_h h_{t-1} + b_h. \quad (56)$$

The Jacobian is

$$J_t = \underbrace{(1 - s)I}_{\text{fixed leak}} + \underbrace{s S_t^h U_h}_{\text{candidate path}}. \quad (57)$$

Unlike DiagGate and SharedGate, there are no gate sensitivities because s is constant and not learned. The dynamics are a rigid combination of identity and the candidate path, with a fixed leakage rate $(1 - s)$ applied to all neurons.

Effective learning rates. Because s is constant, the envelope is trivial:

$$\gamma_{t,\ell}^{(0)} = (1-s)^{t-\ell},$$

identical for all neurons. Thus

$$\mu_{t,\ell}^{(q)} = \mu \left((1-s)^{t-\ell} + \gamma_{t,\ell}^{(1,q)} \right),$$

with $\gamma_{t,\ell}^{(1,q)}$ depending only on the candidate-path correction.

C Noise floor of the empirical matched statistic

This appendix clarifies the assumptions underlying the noise model used in the manuscript and justifies the scaling of stochastic fluctuations in the empirical matched statistic. The key distinction is between exact finite-sample distributions and domain-of-attraction arguments, which suffice to characterize scaling behavior. Throughout, we rely on the linearity of the matched statistic and on standard properties of heavy-tailed random variables [38].

By construction, the empirical matched statistic at lag ℓ is an average over N independent training sequences,

$$\widehat{S}_N(\ell) = \frac{1}{N} \sum_{n=1}^N S_{t,\ell}^{(n)},$$

where $S_{t,\ell}^{(n)}$ denotes the statistic computed from the n th sequence. Independence across sequences implies that the summands are independent for fixed (t, ℓ) . Empirical studies of stochastic gradients in deep neural networks consistently report heavy-tailed fluctuations, typically with tail index $\alpha \in (1, 2)$. Accordingly, we assume that the centered per-sequence statistic $S_{t,\ell}^{(n)} - \mathbb{E}[S_{t,\ell}]$ belongs to the domain of attraction of a symmetric α -stable law. This assumption does not require exact $\mathcal{S}\alpha\mathcal{S}$ behavior at finite sample sizes; it only requires regularly varying tails with index α .

The matched statistic $S_{t,\ell}$ is a finite linear combination of gradient components (Eq. (30)). Linearity preserves the tail index of heavy-tailed variables, so $S_{t,\ell} - \mathbb{E}[S_{t,\ell}]$ also lies in the domain of attraction of a symmetric α -stable law, with a lag-dependent scale parameter $\sigma_\alpha(\ell)$. For analytical convenience, we represent this domain of attraction by a canonical $\mathcal{S}\alpha\mathcal{S}(0, \sigma_\alpha(\ell))$ random variable. Stability under summation then implies

$$\widehat{S}_N(\ell) - \mathbb{E}[S_{t,\ell}] \sim \mathcal{S}\alpha\mathcal{S}\left(0, \sigma_\alpha(\ell)N^{1/\alpha-1}\right) = \mathcal{S}\alpha\mathcal{S}\left(0, \frac{\sigma_\alpha(\ell)}{N^{1-1/\alpha}}\right).$$

Note that the $N^{-1/\alpha}$ scaling applies to sums of α -stable variables, whereas the empirical average introduces an additional factor $1/N$, yielding the rate $N^{-(1-1/\alpha)}$. Thus, the typical magnitude of stochastic fluctuations decays as $N^{-(1-1/\alpha)}$. For $\alpha = 2$ this recovers the classical Gaussian rate $N^{-1/2}$, while for $\alpha < 2$ concentration is slower due to heavy-tailed noise. This noise floor determines the detectability thresholds and sample-complexity bounds derived in the manuscript and underlies the compression of the learnability window in the heavy-tailed regime.

D LAN-based KL bound for averaged α -stable location models

For completeness, we derive the KL lower bound used in Section 5.3.2 for the empirical matched statistic $\widehat{S}_N(\ell)$, which is defined as an average over N independent training sequences. Unlike the classical LAN setting for product measures, the present analysis concerns a *shrinking-scale* α -stable location family. The argument follows the general LAN framework for triangular arrays of statistical experiments with vanishing noise levels [48].

Statistical model and parameterization. We consider the statistical experiment induced by the empirical matched statistic $\widehat{S}_N(\ell)$ at a fixed lag ℓ , which is defined as an average over N independent training sequences. As shown in Appendix C, under heavy-tailed gradient fluctuations with tail index $\alpha > 1$, the centered statistic $\widehat{S}_N(\ell) - \mathbb{E}[S_{t,\ell}]$ exhibits stochastic fluctuations whose typical magnitude scales as $N^{-(1-1/\alpha)}$.

To formalize hypothesis testing at lag ℓ , we model the distribution of the centered empirical statistic by a location family with shrinking scale. Specifically, let Z be a symmetric α -stable random variable with unit scale and characteristic exponent $\alpha > 1$, and define the observation

$$Y_N = \theta + s_N Z, \quad s_N := \sigma_\alpha(\ell) N^{1/\alpha-1}. \quad (58)$$

Here, Y_N represents the random fluctuation of the empirical matched statistic, and $\theta \in \mathbb{R}$ is a location parameter encoding the presence or absence of a lag- ℓ dependency.

In the detection problem considered in the main text, θ corresponds to the mean shift induced by the effective learning rate alignment:

$$\theta \in \left\{ +\frac{1}{2}\Delta(\ell), -\frac{1}{2}\Delta(\ell) \right\}, \quad \Delta(\ell) = \overline{m}_\mu(\ell) f(\ell).$$

Thus, the two hypotheses differ only by a small location perturbation whose magnitude is controlled by the effective learning-rate envelope.

For $\alpha > 1$, symmetric α -stable laws are absolutely continuous and admit a density. Denoting by $P_{\theta,N}$ the law of Y_N , its density is given by

$$p_{\theta,N}(y) = \frac{1}{s_N} f_0\left(\frac{y-\theta}{s_N}\right), \quad (59)$$

where f_0 is the density of a fixed symmetric α -stable distribution with unit scale.

Triangular-array structure and relation to classical LAN. Unlike the classical LAN framework, which considers N i.i.d. observations from a fixed distribution, the present setting involves a *triangular array* of statistical experiments. This means that for each sample size N we observe a *single* random variable Y_N , whose distribution depends on N through the shrinking scale s_N .

Intuitively, this structure arises because $\widehat{S}_N(\ell)$ is itself an average over N independent sequences: increasing N does not provide more independent observations of a fixed noise model, but instead produces a more concentrated version of the same statistic. As N grows, the noise scale s_N tends to zero, yielding a sequence of location families with vanishing dispersion.

Such shrinking-scale location models are a standard object in asymptotic statistics [48] and admit local asymptotic normality under mild regularity conditions. In the present case, for $\alpha > 1$, the family $\{P_{\theta,N}\}_{N \geq 1}$ satisfies a LAN expansion with normalization rate $r_N = s_N^{-1}$.

LAN for shrinking-scale location families. For $\alpha > 1$, symmetric α -stable densities possess finite Fisher information for the location parameter [21, 30, 38, 48]. As $s_N \rightarrow 0$, the family $\{P_{\theta,N}\}_{N \geq 1}$ forms a triangular array of location models that is locally asymptotically normal with normalization rate

$$r_N := \frac{1}{s_N} = \frac{N^{1-1/\alpha}}{\sigma_\alpha(\ell)}.$$

Specifically, there exists a constant $I_\alpha > 0$, depending only on the tail index α , and a sequence of random variables Δ_N such that, for each fixed $h \in \mathbb{R}$,

$$\log \frac{dP_{\theta+h/r_N,N}}{dP_{\theta,N}} = h \Delta_N - \frac{1}{2} h^2 I_\alpha + o_{P_{\theta,N}}(1), \quad \Delta_N \xrightarrow{d} \mathcal{N}(0, I_\alpha), \quad (60)$$

as $N \rightarrow \infty$. The constant I_α plays the role of an effective information coefficient in the local asymptotic expansion and does not require an explicit expression.

Taking expectations with respect to $P_{\theta,N}$ and using $\mathbb{E}[\Delta_N] = 0$ yields the asymptotic expansion of the KL divergence [30]:

$$D_{\text{KL}}(P_{\theta+h/r_N,N} \| P_{\theta,N}) = \frac{1}{2}h^2 I_\alpha + o(1). \quad (61)$$

Consequently, for all sufficiently large N , there exists a constant $c_\alpha > 0$ such that

$$D_{\text{KL}}(P_{\theta+h/r_N,N} \| P_{\theta,N}) \geq c_\alpha h^2. \quad (62)$$

Application to the detection problem in the main text. In the main text, the detection and non-detection hypotheses correspond to two symmetric location parameters separated by a fixed amount $\Delta(\ell)$:

$$\theta_1 = +\frac{1}{2}\Delta(\ell), \quad \theta_0 = -\frac{1}{2}\Delta(\ell),$$

so that $\theta_1 - \theta_0 = \Delta(\ell)$.

The empirical matched statistic has a shrinking noise scale $s_N = \sigma_\alpha(\ell)N^{1/\alpha-1}$ (Appendix C). To express the fixed separation in the LAN framework, we measure it in units of this scale and define the normalized separation

$$h_N := \frac{\theta_1 - \theta_0}{s_N} = \frac{N^{1-1/\alpha} \Delta(\ell)}{\sigma_\alpha(\ell)}.$$

Substituting $h = h_N$ into the LAN-based KL lower bound (62) yields

$$D_{\text{KL}}(P_{\text{det}} \| P_{\text{non}}) \geq c_\alpha h_N^2 = c_\alpha \frac{N^{2(1-1/\alpha)} \Delta(\ell)^2}{\sigma_\alpha(\ell)^2}, \quad (63)$$

which is exactly the bound used in Eq. (34) of the main text.

E From KL divergence to mutual information and Fano bounds

This appendix provides a self-contained derivation of the mutual information lower bound and the Fano-type sample complexity inequality used in Sec. 5.3.2. The arguments rely only on standard relations between KL divergence, mutual information, and binary hypothesis testing [11].

Binary detection setup. Fix a lag ℓ . The hypotheses in Sec. 5.3.2 correspond to two α -stable location models for the empirical matched statistic $S = \widehat{S}_N(\ell)$, obtained by averaging over N independent training sequences. Introduce a binary label

$$B \in \{0, 1\}, \quad \mathbb{P}(B=1) = \mathbb{P}(B=0) = \frac{1}{2},$$

where $B=1$ selects the *detection* distribution P_{det} and $B=0$ selects the *non-detection* distribution P_{non} . The mutual information between B and S is defined as

$$I(B; S) = D_{\text{KL}}(P_{B,S} \| P_B P_S),$$

where $P_{B,S}$ denotes the joint distribution and $P_B P_S$ the product of the marginals.

Mutual information via the mixture identity. Because B is equiprobable, the joint density factorizes as

$$p_{B,S}(b, s) = p_B(b) p_{S|B}(s | b) = \frac{1}{2} p_{S|B}(s | b),$$

with

$$p_{S|B}(s | 1) = p_{\text{det}}(s), \quad p_{S|B}(s | 0) = p_{\text{non}}(s).$$

The marginal distribution of S is the mixture

$$M = \frac{1}{2}P_{\text{det}} + \frac{1}{2}P_{\text{non}}.$$

Starting from the definition of mutual information,

$$I(B; S) = \sum_{b=0}^1 \int p_B(b) p_{S|B}(s | b) \log \frac{p_{S|B}(s | b)}{p_S(s)} dt,$$

one obtains the mixture identity

$$I(B; S) = \frac{1}{2} D_{\text{KL}}(P_{\text{det}} \| M) + \frac{1}{2} D_{\text{KL}}(P_{\text{non}} \| M). \quad (64)$$

Since KL divergences are nonnegative,

$$I(B; S) \geq \frac{1}{2} D_{\text{KL}}(P_{\text{det}} \| M),$$

and since mutual information cannot exceed the entropy of the binary label, $I(B; S) \leq \log 2$. Combining these observations yields the general lower bound

$$I(B; S) \geq \min\{\log 2, \frac{1}{2} D_{\text{KL}}(P_{\text{det}} \| M)\}. \quad (65)$$

In the main text, the factor $\frac{1}{2}$ and the difference between $D_{\text{KL}}(P_{\text{det}} \| M)$ and $D_{\text{KL}}(P_{\text{det}} \| P_{\text{non}})$ are absorbed into the constant c_α , since only the scaling with respect to N and $\Delta(\ell)/\sigma_\alpha(\ell)$ is relevant.

Fano's inequality and sample complexity. Let P_e denote the probability of incorrectly deciding whether a lag- ℓ signal is present based on the observation of S . For binary hypotheses with equal priors, Fano's inequality [11] gives

$$P_e \geq 1 - \frac{I(B; S)}{\log 2}.$$

Thus, to ensure a target error probability $P_e \leq \epsilon < 1/2$, it is sufficient that

$$I(B; S) \geq \log 2 (1 - \epsilon).$$

Substituting the mutual-information lower bound from Eq. (35) and solving for N yields the sample complexity inequality

$$N \geq \left(\frac{\sigma_\alpha(\ell)}{\sqrt{c_\alpha} \bar{m}_\mu(\ell) f(\ell)} \right)^{\frac{\alpha}{\alpha-1}} \left(\log \frac{1}{2\epsilon} \right)^{\frac{\alpha}{2(\alpha-1)}}, \quad (66)$$

which is the bound reported in Sec. 5.3.2.

F Proofs of Lemmas

Proof of Lemma 5.1

Proof. Recall that for the diagonally gated models in Appendix B we write $\mu_{t,\ell}^{(q)} = \mu(\gamma_{t,\ell}^{(0,q)} + \gamma_{t,\ell}^{(1,q)})$, while for the GRU we additionally track the diagonal zeroth-order envelopes $\gamma_{t,\ell}^{(0,q)}$, $\rho_{t,\ell}^{(0,q)}$, $\eta_{t,\ell}^{(0,q)}$ (see Eq. (26)); the LSTM zeroth-order coefficient is given by Eq. (13). In all cases, the *zeroth-order* diagonal envelopes are products of time-local gate factors and bounded activation derivatives, hence lie in $[0, 1]$.

Since $\mu_{t,\ell}^{(q)}$ may receive signed contributions from recurrent weights in the first-order correction, and since detectability depends on signal magnitude rather than orientation, we establish monotonicity for the envelope

$$f(\ell) := \sum_{q=1}^H |\mu_{t,\ell}^{(q)}|.$$

Zeroth order. For the diagonally gated RNNs in Appendix B, for each neuron q the zeroth-order term admits the lag representation

$$\gamma_{t,\ell}^{(0,q)} = \prod_{k=0}^{\ell-1} a_{t-k}^{(q)}, \quad a_{t-k}^{(q)} \in [0, 1],$$

so that

$$\gamma_{t,\ell+1}^{(0,q)} = \gamma_{t,\ell}^{(0,q)} a_{t-\ell}^{(q)} \leq \gamma_{t,\ell}^{(0,q)}.$$

For the GRU, the additional envelopes

$$\rho_{t,\ell}^{(0,q)} = \prod_{k=0}^{\ell-1} r_{t-k,q}, \quad \eta_{t,\ell}^{(0,q)} = \prod_{k=0}^{\ell-1} (1 - z_{t-k,q}) r_{t-k,q}$$

obey the same multiplicative extension property and are therefore nonincreasing in ℓ .

For the LSTM, Eq. (13) yields the single surviving zeroth-order path

$$\gamma_{t,\ell}^{(0,q)} = e_{t,q} \prod_{k=1}^{\ell} f_{t-k+1,q}, \quad e_{t,q} \in [0, 1], \quad f_{t-k+1,q} \in [0, 1],$$

which is again nonincreasing as ℓ increases.

First-order diagonal correction. Fix q . The diagonal first-order term is a finite sum of contributions indexed by the insertion time p (and, in general, by a finite set of diagonal factors produced by the architecture at time p). Each such contribution has the form

$$C_{p,t,\ell}^{(q)} = b_p^{(q)} \prod_{j \in \mathcal{I}_{p,\ell}} a_j^{(q)}, \quad a_j^{(q)} \in [0, 1],$$

where $b_p^{(q)}$ is ℓ -independent (possibly signed), and where the index sets satisfy $\mathcal{I}_{p,\ell} \subseteq \mathcal{I}_{p,\ell+1}$ (i.e. increasing the lag can only add further multiplicative gate factors). Therefore,

$$|C_{p,t,\ell+1}^{(q)}| = |C_{p,t,\ell}^{(q)}| a_{t-\ell}^{(q)} \leq |C_{p,t,\ell}^{(q)}|,$$

and by summing over the finitely many contributions we obtain that $\ell \mapsto |\gamma_{t,\ell}^{(1,q)}|$ is nonincreasing.

Conclusion. By the triangle inequality,

$$|\mu_{t,\ell}^{(q)}| = \mu |\gamma_{t,\ell}^{(0,q)} + \gamma_{t,\ell}^{(1,q)}| \leq \mu \left(\gamma_{t,\ell}^{(0,q)} + |\gamma_{t,\ell}^{(1,q)}| \right),$$

and the right-hand side is a sum of nonnegative, nonincreasing terms in ℓ . Summing over q shows that $f(\ell) = \sum_q |\mu_{t,\ell}^{(q)}|$ is nonincreasing. \square

Proof of Lemma 5.2

Proof. Starting from the per-lag sufficient sample size in Eq. (40),

$$N(\ell) = \kappa_{\alpha,\epsilon} \left(\frac{\sigma_{\alpha}(\ell)}{\bar{m}_{\mu}(\ell) f(\ell)} \right)^{\kappa_{\alpha}}, \quad \kappa_{\alpha,\epsilon} = \frac{1}{c_{\alpha}^{\kappa_{\alpha}/2}} \left(\log \frac{1}{2\epsilon} \right)^{\kappa_{\alpha}/2},$$

and applying the boundedness assumptions $c_{\sigma} \leq \sigma_{\alpha}(\ell) \leq C_{\sigma}$ and $c_m \leq \bar{m}_{\mu}(\ell) \leq C_m$, we obtain

$$\kappa_{\alpha,\epsilon} \left(\frac{c_{\sigma}}{C_m} \right)^{\kappa_{\alpha}} f(\ell)^{-\kappa_{\alpha}} \leq N(\ell) \leq \kappa_{\alpha,\epsilon} \left(\frac{C_{\sigma}}{c_m} \right)^{\kappa_{\alpha}} f(\ell)^{-\kappa_{\alpha}},$$

which yields Eq. (41) with $c_\star = \kappa_{\alpha,\epsilon}(c_\sigma/C_m)^{\kappa_\alpha}$ and $C_\star = \kappa_{\alpha,\epsilon}(C_\sigma/c_m)^{\kappa_\alpha}$.

For the horizon bound, recall the detectability condition from Eq. (38):

$$f(\ell) \geq \frac{\sigma_\alpha(\ell)}{N^{1/\kappa_\alpha} \bar{m}_\mu(\ell)}.$$

As before, the constant factor $\frac{1}{\sqrt{c_\alpha}} \sqrt{\log \frac{1}{2\epsilon}}$ is independent of ℓ and N and can be absorbed into the constants of the sandwich bound.

Bounding the right-hand side above and below using the assumed bounds on $\sigma_\alpha(\ell)$ and $\bar{m}_\mu(\ell)$ gives

$$\frac{c_\sigma}{C_m} N^{-1/\kappa_\alpha} \leq \frac{\sigma_\alpha(\ell)}{N^{1/\kappa_\alpha} \bar{m}_\mu(\ell)} \leq \frac{C_\sigma}{c_m} N^{-1/\kappa_\alpha}.$$

The detectability condition is guaranteed whenever

$$f(\ell) \geq \frac{C_\sigma}{c_m} N^{-1/\kappa_\alpha},$$

and cannot hold unless

$$f(\ell) \geq \frac{c_\sigma}{C_m} N^{-1/\kappa_\alpha}.$$

Since $f(\ell)$ is nonincreasing (Lemma 5.1), the admissible lags form an interval $[0, f^\leftarrow(x)]$. Applying the generalized inverse f^\leftarrow yields

$$f^\leftarrow\left(\frac{C_\sigma}{c_m} N^{-1/\kappa_\alpha}\right) \leq \mathcal{H}_N \leq f^\leftarrow\left(\frac{c_\sigma}{C_m} N^{-1/\kappa_\alpha}\right),$$

which establishes the claimed sandwich bound. \square

Generalized inverse. The generalized inverse is used because $f(\ell)$ need not be strictly decreasing. By Lemma 5.1, $f(\ell)$ is nonincreasing, ensuring that f^\leftarrow is well defined. The proof shows that the dependence on stochasticity and alignment enters only through the constants $(c_\sigma, C_\sigma, c_m, C_m)$ and the tail index α (via κ_α); the functional dependence of $N(\ell)$ and \mathcal{H}_N on the envelope $f(\ell)$ is dictated entirely by the power $f(\ell)^{-\kappa_\alpha}$.

On the boundedness assumptions. The conditions $c_\sigma \leq \sigma_\alpha(\ell) \leq C_\sigma$ and $c_m \leq \bar{m}_\mu(\ell) \leq C_m$ should be understood as mild regularity assumptions over the finite range of lags under consideration. Absent pathological degeneracies, such as vanishing alignment $\bar{m}_\mu(\ell) \rightarrow 0$ or diverging fluctuation scale $\sigma_\alpha(\ell) \rightarrow \infty$, these quantities remain finite and vary smoothly with ℓ . Thus, the boundedness assumptions affect only constant factors in Eq. (41), while the asymptotic dependence of $N(\ell)$ and \mathcal{H}_N on the envelope $f(\ell)$ is entirely captured by the exponent κ_α .

G Asymptotic Scaling of the Learnability Window under α -Stable Noise

This appendix provides the detailed derivations supporting the scaling relations summarized in Sec. 5.4 and established by Lemmas 5.1–5.2. Throughout, we use the corrected concentration exponent $\kappa_\alpha = \alpha/(\alpha - 1)$, which governs the statistical behavior of empirical averages under α -stable noise. Starting from the α -stable model of Eq. (33) and the finite-sample bound of Eq. (36), we show how the slow N^{1/κ_α} concentration rate characteristic of heavy-tailed averages determines the asymptotic growth of the learnability window \mathcal{H}_N .

Per-lag sufficient sample size. From Eq. (36), the minimal number of independent sequences required to detect a lag- ℓ dependency with error probability $P_e \leq \epsilon$ is

$$N(\ell) = \kappa_{\alpha, \epsilon} \left(\frac{\sigma_\alpha(\ell)}{\bar{m}_\mu(\ell) f(\ell)} \right)^{\kappa_\alpha}, \quad \kappa_{\alpha, \epsilon} = \frac{1}{C_\alpha^{\kappa_\alpha/2}} \left(\log \frac{1}{2\epsilon} \right)^{\kappa_\alpha/2}. \quad (67)$$

The constant $\kappa_{\alpha, \epsilon}$ depends only on the tail index α and the target detection error ϵ , and can be absorbed into the asymptotic constants below. We assume the boundedness conditions of Lemma 5.2,

$$c_\sigma \leq \sigma_\alpha(\ell) \leq C_\sigma, \quad c_m \leq \bar{m}_\mu(\ell) \leq C_m,$$

and recall that $\ell \mapsto f(\ell)$ is nonincreasing (Lemma 5.1).

Two-sided sandwich bound. Substituting these bounds into (67) yields constants

$$c_\star := \kappa_{\alpha, \epsilon} \left(\frac{c_\sigma}{C_m} \right)^{\kappa_\alpha}, \quad C_\star := \kappa_{\alpha, \epsilon} \left(\frac{C_\sigma}{c_m} \right)^{\kappa_\alpha},$$

such that

$$c_\star f(\ell)^{-\kappa_\alpha} \leq N(\ell) \leq C_\star f(\ell)^{-\kappa_\alpha}. \quad (68)$$

Hence,

$$N(\ell) \propto f(\ell)^{-\kappa_\alpha} \quad (69)$$

gives the *master proportionality relation* between the minimum sample size and the envelope, formalizing that longer dependencies (smaller $f(\ell)$) require increasingly large sample sizes to detect under heavy-tailed noise.

Learnability window as a level set. From the finite-sample detectability condition of Eq. (38),

$$f(\ell) \geq \frac{\sigma_\alpha(\ell)}{N^{1/\kappa_\alpha} \bar{m}_\mu(\ell)},$$

and using the same bounding arguments, we can express the learnability window \mathcal{H}_N as a level set of $f(\ell)$:

$$f^\leftarrow\left(\frac{C_\sigma}{c_m} N^{-1/\kappa_\alpha}\right) \leq \mathcal{H}_N \leq f^\leftarrow\left(\frac{c_\sigma}{C_m} N^{-1/\kappa_\alpha}\right), \quad (70)$$

where $f^\leftarrow(y) = \sup\{\ell \geq 1 : f(\ell) \geq y\}$ denotes the generalized inverse. By Lemma 5.1, $f(\ell)$ is nonincreasing, ensuring that the generalized inverse f^\leftarrow is well-defined. This reproduces the sandwich bound in Eq. (42) of the main text.

Asymptotic regimes. Considering the master proportionality in Eq. 69, we now invert (68) (equivalently (70)) for three canonical decay laws of the envelope $f(\ell)$.

(i) **Logarithmic decay.** If $f(\ell) \asymp c/\log(1+\ell)$ with $c > 0$, then

$$N(\ell) \asymp [\log(1+\ell)]^{\kappa_\alpha} \implies \log(1+\ell) \asymp N^{1/\kappa_\alpha} \implies \mathcal{H}_N \asymp \exp(\kappa N^{1/\kappa_\alpha}) - 1.$$

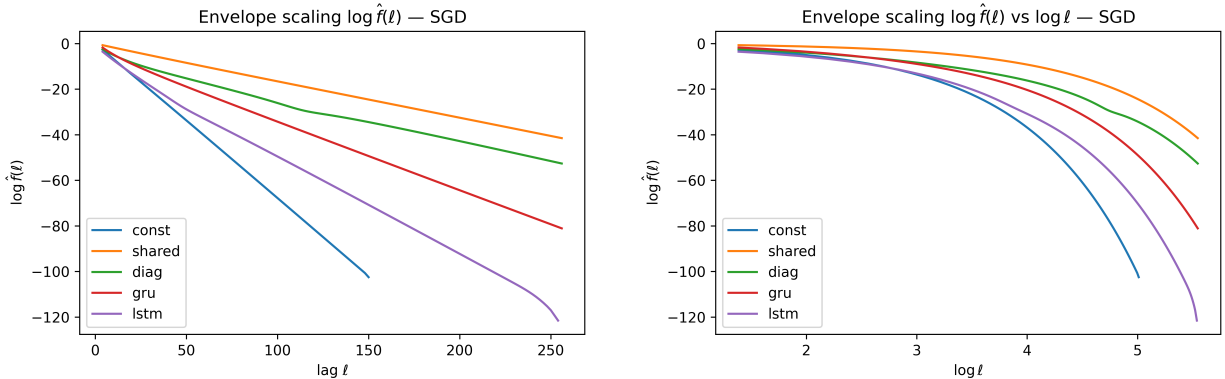
(ii) **Polynomial (algebraic) decay.** If $f(\ell) \asymp c\ell^{-\beta}$ with $\beta > 0$, then

$$N(\ell) \asymp \ell^{\kappa_\alpha \beta} \implies \mathcal{H}_N \asymp N^{1/(\kappa_\alpha \beta)}.$$

(iii) **Exponential (geometric) decay.** If $f(\ell) \asymp c\lambda^\ell$ with $\lambda \in (0, 1)$, then

$$N(\ell) \asymp \lambda^{-\kappa_\alpha \ell} \implies \mathcal{H}_N \asymp \frac{\log N}{\kappa_\alpha \log(1/\lambda)}.$$

All asymptotic forms hold up to multiplicative constants inherited from c_σ , C_σ , c_m , C_m , and $\kappa_{\alpha, \epsilon}$. As α decreases, heavier tails increase κ_α and slow the N^{1/κ_α} concentration of empirical averages, uniformly compressing the learnability window \mathcal{H}_N across all decay regimes.



(a) Semi-log scaling of $\hat{f}(\ell)$.

(b) Log-log scaling of $\hat{f}(\ell)$.

Figure 6: Plain SGD: envelope scaling diagnostics for $\hat{f}(\ell)$.

H Optimizer dependence of envelope scaling and time-scale spectra

This appendix reports additional experiments performed with plain SGD and SGD with momentum, complementing the main-text results obtained with AdamW. Our framework predicts that architectural design and optimization dynamics jointly shape the coupled state-parameter system and may bias training toward different effective time-scale regimes. However, it does not require that a single regime be universally realized across optimizers, tasks, or training configurations.

In particular, the emergence of broad mixtures of effective time scales depends on the interaction between architecture, optimizer, sequence length, task structure, and training hyperparameters. Different configurations may therefore lead to qualitatively different envelope behavior even under the same optimizer. The results below document one consistent realization of the diagnostic pipeline under SGD-like dynamics, without asserting optimizer-specific regimes.

Plain SGD. Under plain SGD, the estimated envelope $\hat{f}(\ell)$ exhibits clear exponential decay for all architectures (Fig. 6). Semi-log fits achieve near-perfect linearity ($R^2 > 0.99$), whereas log-log fits are substantially weaker, indicating that curvature in log-log coordinates reflects finite-range effects rather than genuine scale-free behavior. The inferred exponential rates are finite and architecture-dependent, with slower decay for SharedGate and DiagGate than for ConstGate.

Consistently, the time-scale spectra remain bounded (Fig. 7), supporting a finite-memory exponential regime under plain SGD in the present setting.

Noise statistics: plain SGD. We estimated the tail index $\hat{\alpha}(\ell)$ and the associated noise scale $\hat{\sigma}_\alpha(\ell)$ across diagnostic lags. While several architectures retain substantial mass in the heavy-tailed regime ($\hat{\alpha} \approx 1.1$ – 1.3), the distributions also exhibit non-negligible mass near the Gaussian limit $\alpha = 2$ (Fig. 8a), indicating partial re-Gaussianization under plain SGD in the present configuration.

The noise scale $\hat{\sigma}_\alpha(\ell)$ decays rapidly with lag (Fig. 8b), more strongly than observed under AdamW. This accelerated attenuation of gradient fluctuations is consistent with the finite-memory exponential envelope regime identified above.

Overall, plain SGD does not eliminate heavy-tailed behavior entirely, but it exhibits weaker and more rapidly attenuating tail effects compared to the AdamW setting. The concentration properties therefore remain compatible with the theoretical framework, albeit with reduced heavy-tailed persistence.

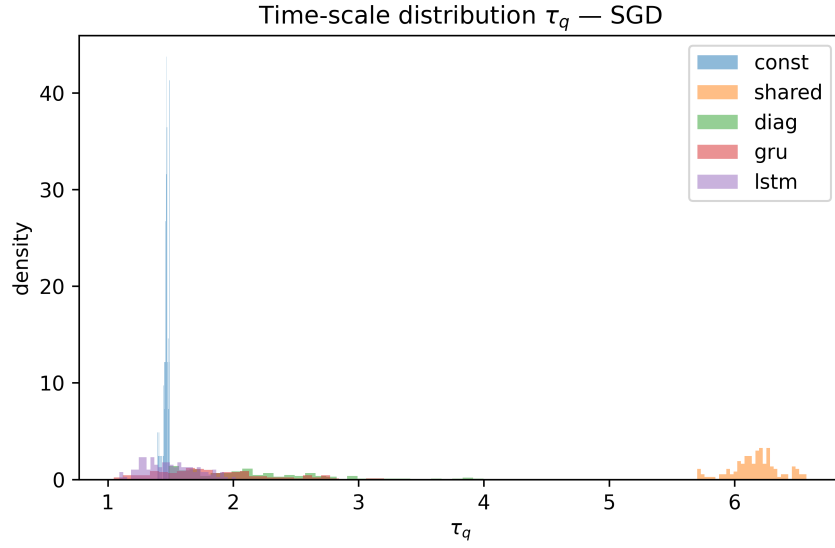
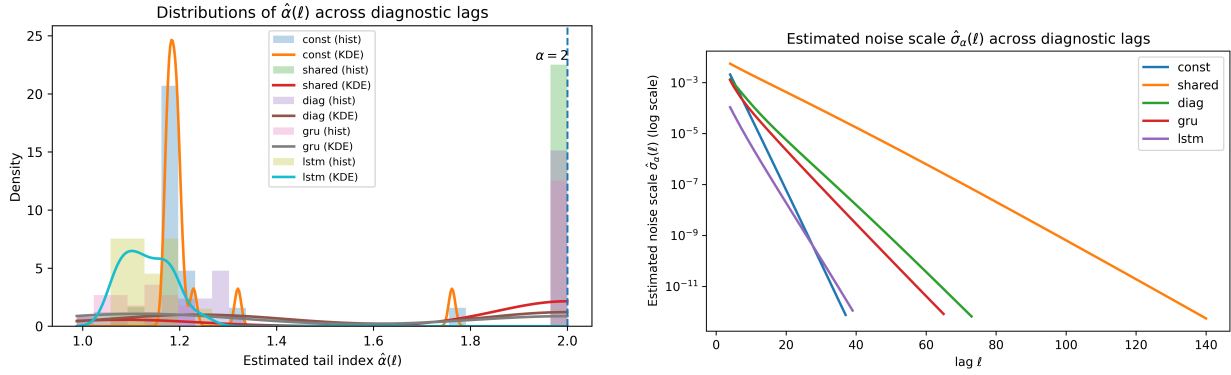


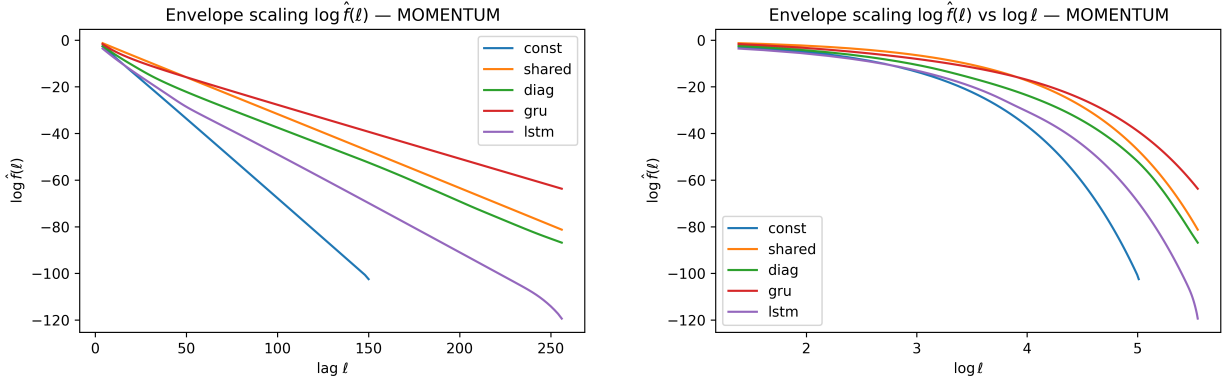
Figure 7: Plain SGD: time-scale spectra τ_q . All architectures exhibit bounded support, consistent with exponential envelope decay.



(a) Distribution of $\hat{\alpha}(\ell)$ under plain SGD.

(b) Noise scale $\hat{\sigma}_\alpha(\ell)$ under plain SGD (log scale).

Figure 8: Noise diagnostics under plain SGD.



(a) Semi-log scaling of $\hat{f}(\ell)$ under momentum.

(b) Log-log scaling of $\hat{f}(\ell)$ under momentum.

Figure 9: SGD with momentum: envelope scaling diagnostics.

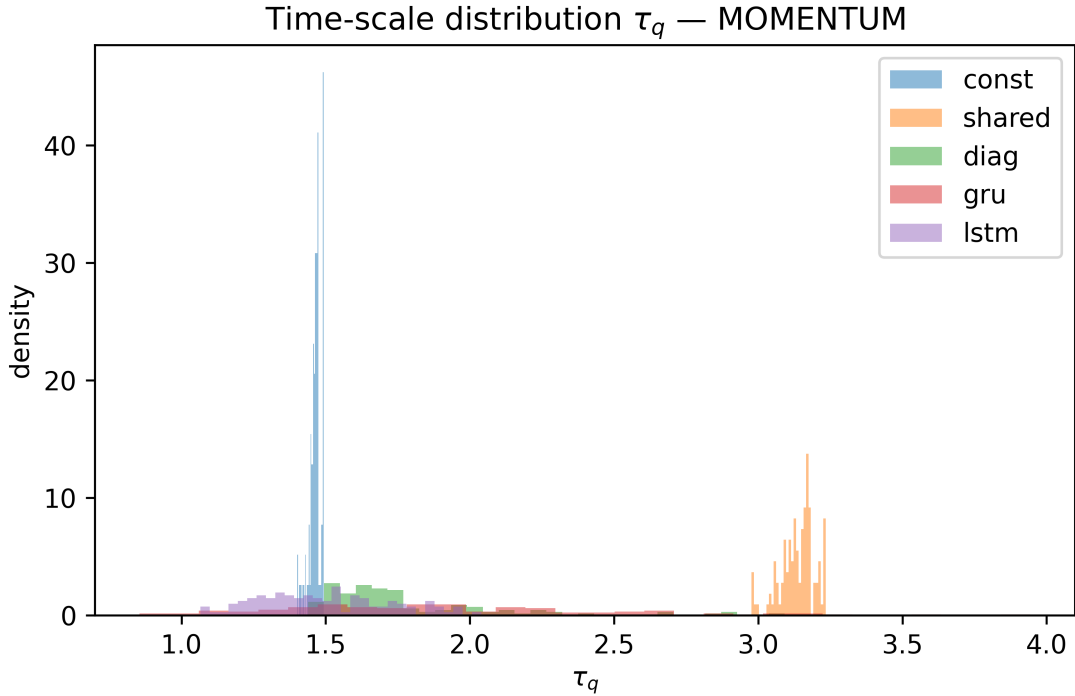
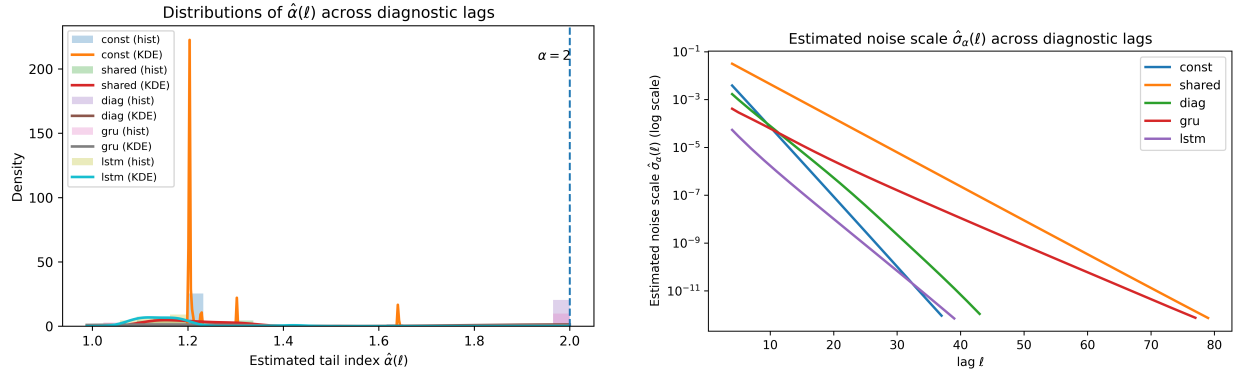


Figure 10: SGD with momentum: unit-level time-scale spectra τ_q .

SGD with momentum. Under SGD with momentum, the envelope $\hat{f}(\ell)$ remains exponentially attenuated across architectures (Fig. 9). Semi-log fits again achieve near-perfect linearity ($R^2 > 0.998$), while log-log fits are substantially weaker, indicating the absence of genuine polynomial decay on the tested horizon. Momentum modifies the characteristic exponential rates but does not induce a qualitative change of regime.

The corresponding time-scale spectra remain bounded (Fig. 10). Although characteristic time scales shift relative to plain SGD, no heavy-tailed or unbounded τ_q distribution emerges. Thus, SGD with momentum also resides in a finite-memory exponential regime in the present setting.



(a) Distribution of $\hat{\alpha}(\ell)$ under momentum.

(b) Noise scale $\hat{\sigma}_\alpha(\ell)$ under momentum (log scale).

Figure 11: Noise diagnostics under SGD with momentum.

Noise statistics: SGD with momentum. The estimated tail indices remain heavy-tailed and well separated from the Gaussian limit (Fig. 11a). The noise scale $\hat{\sigma}_\alpha(\ell)$ decays smoothly with lag (Fig. 11b) without optimizer-induced regime transitions.

Therefore, although momentum alters effective decay rates and shifts characteristic time scales, it does not modify the underlying heavy-tailed noise class in the present configuration. Observed differences in envelope behavior primarily reflect changes in effective time-scale geometry rather than transitions in statistical concentration properties.

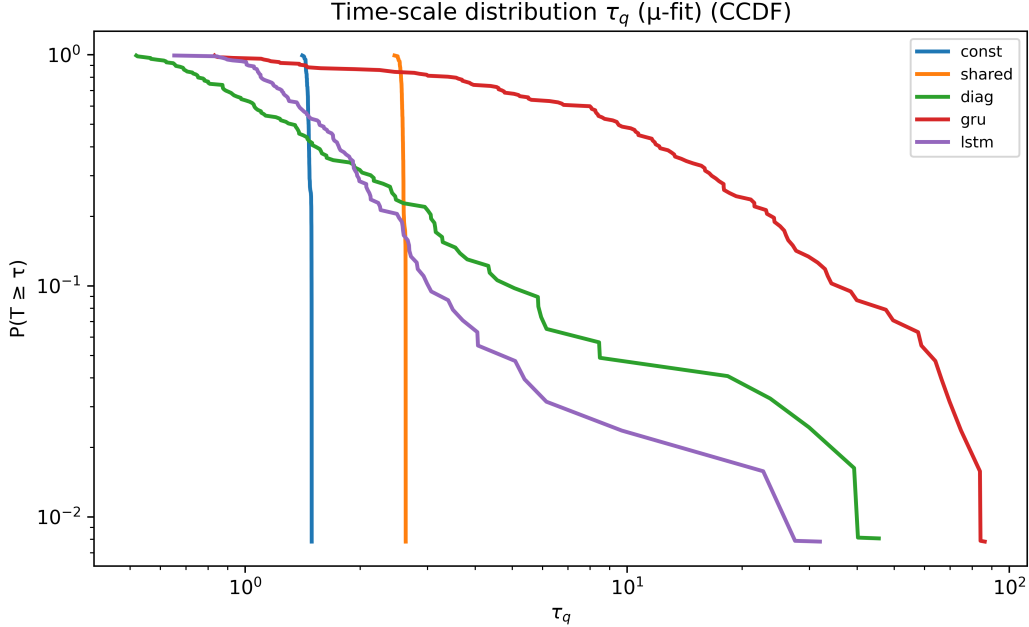
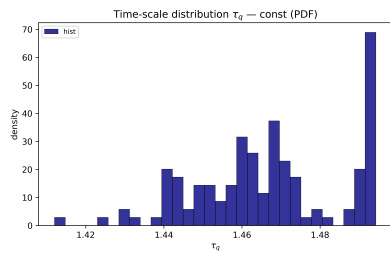


Figure 12: Log–log representation of the CCDF of neuronwise time scales τ_q . DiagGate, GRU, and LSTM exhibit extended intermediate tails with eventual attenuation, whereas ConstGate and SharedGate are tightly concentrated.

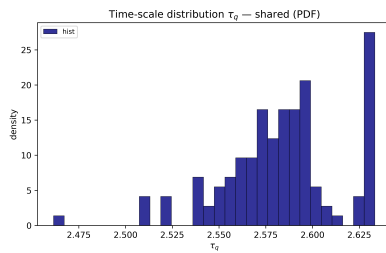
I Additional time-scale spectrum diagnostics

Tail-emphasis representation. To further examine the slow end of the time-scale spectra, Fig. 12 reports the complementary cumulative distribution functions (CCDFs) on log–log axes. This representation emphasizes differences in intermediate and large time scales. ConstGate and SharedGate exhibit sharply truncated spectra, with negligible mass beyond a narrow range of τ . In contrast, DiagGate, GRU, and LSTM display extended intermediate ranges over which the CCDF decays slowly, followed by a clear attenuation at the largest observed τ . While these intermediate regimes may appear approximately linear over limited ranges, the eventual curvature confirms that the distributions are not asymptotically scale-invariant, but instead reflect a mixed multi-scale regime with an effective finite-size cut-off.

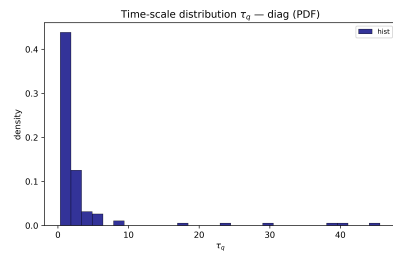
Per-model distributions. For completeness, Fig. 13 shows the empirical probability density functions (histograms) of τ_q for each model. ConstGate and SharedGate produce narrowly concentrated spectra, consistent with their homogeneous gating geometry. DiagGate exhibits a visibly heterogeneous mixture, with a majority of short time scales and a smaller subpopulation of substantially longer ones. GRU and LSTM display broader and more gradually decaying spectra, indicating richer mixtures of effective memory depths. These density-level diagnostics reinforce the CCDF-based conclusions reported in Sec. 6 and confirm that envelope geometry and learnability horizon are tightly linked to the dispersion of neuronwise time scales.



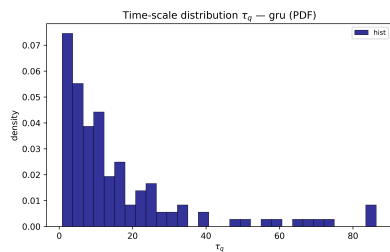
(a) ConstGate



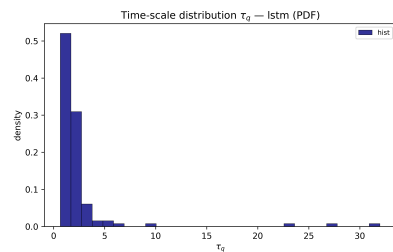
(b) SharedGate



(c) DiagGate



(d) GRU



(e) LSTM

Figure 13: Empirical probability density functions of neuronwise time scales τ_q . DiagGate, GRU, and LSTM exhibit visibly broader and more heterogeneous spectra than ConstGate and SharedGate.

References

- [1] M. Arjovsky, A. Shah, and Y. Bengio. Unitary evolution recurrent neural networks. In *International Conference on Machine Learning*, pages 1120–1128, New York, USA, June 2016.
- [2] D. G. Barrett and B. Dherin. Implicit gradient regularization. In *International Conference on Learning Representations*, 2021.
- [3] Y. Bengio, P. Simard, and P. Frasconi. Learning long-term dependencies with gradient descent is difficult. *IEEE Transactions on Neural Networks*, 5(2):157–166, 1994. doi: 10.1109/72.279181.
- [4] B. Chang, L. Meng, E. Haber, L. Ruthotto, D. Begert, and E. Holtham. Antisymmetricrnn: A dynamical system view on recurrent neural networks. In *International Conference on Learning Representations*, 2019.
- [5] S. Chang, Y. Zhang, W. Han, M. Yu, X. Guo, W. Tan, X. Cui, M. Witbrock, M. Hasegawa-Johnson, and T. S. Huang. Dilated recurrent neural networks. In *Advances in Neural Information Processing Systems*, 2017.
- [6] M. Chen, J. Pennington, and S. S. Schoenholz. Dynamical isometry and a mean field theory of RNNs: Gating enables signal propagation in recurrent neural networks. In *Proceedings of the 35th International Conference on Machine Learning*, pages 872–881, 2018.
- [7] S. Chezhegov, K. Yaroslav, A. Semenov, A. Beznosikov, A. Gasnikov, S. Horváth, M. Takáč, and E. Gorbunov. Clipping improves Adam-norm and AdaGrad-norm when the noise is heavy-tailed. In A. Singh, M. Fazel, D. Hsu, S. Lacoste-Julien, F. Berkenkamp, T. Maharaj, K. Wagstaff, and J. Zhu, editors, *Proceedings of the 42nd International Conference on Machine Learning*, volume 267 of *Proceedings of Machine Learning Research*, pages 10269–10333. PMLR, 13–19 Jul 2025. URL <https://proceedings.mlr.press/v267/chezhegov25a.html>.
- [8] K. Cho, B. Van Merriënboer, D. Bahdanau, and Y. Bengio. On the properties of neural machine translation: Encoder-decoder approaches. *arXiv preprint arXiv:1409.1259*, 2014.
- [9] J. Chung, S. Ahn, and Y. Bengio. Hierarchical multiscale recurrent neural networks. In *International Conference on Learning Representations*, Toulon, France, Apr. 2017.
- [10] T. Cooijmans, N. Ballas, C. Laurent, C. Gülçehre, and A. C. Courville. Recurrent batch normalization. In *International Conference on Learning Representations*, 2016.
- [11] T. M. Cover and J. A. Thomas. *Elements of Information Theory*. John Wiley & Sons, New York, NY, 2006. ISBN 9780471241959.
- [12] J. Dambre, D. Verstraeten, B. Schrauwen, and S. Massar. Information processing capacity of dynamical systems. *Scientific Reports*, 2, 2012. doi: 10.1038/srep00514.
- [13] T. Dao, G. Yang, S. L. Smith, and L. Amini. Kernel regime of wide neural networks: Gradient descent dynamics and generalization. In *Advances in Neural Information Processing Systems*, 2021.
- [14] F. A. Gers, J. Schmidhuber, and F. Cummins. Learning to forget: Continual prediction with LSTM. In *Neural Computation*, volume 12, pages 2451–2471, 2000.
- [15] A. Gu, I. Johnson, K. Goel, K. K. Saab, T. Dao, A. Rudra, and C. Ré. Combining recurrent, convolutional, and continuous-time models with linear state space layers. In *Thirty-Fifth Conference on Neural Information Processing Systems*, 2021.
- [16] A. Gu, K. Goel, and C. Ré. Efficiently modeling long sequences with structured state spaces. In *International Conference on Learning Representations*, 2022.

- [17] H. Gupta, H. Mehta, and J. Z. Kolter. Stability and expressivity of implicit recurrent models. In *Advances in Neural Information Processing Systems*, 2022.
- [18] N. J. Higham. *Functions of Matrices: Theory and Computation*. SIAM, 2008.
- [19] S. Hochreiter and J. Schmidhuber. Long short-term memory. *Neural Computation*, 9(8):1735–1780, 1997.
- [20] F. Hübler, I. Fatkhullin, and N. He. From gradient clipping to normalization for heavy tailed SGD, 2025. URL <https://arxiv.org/abs/2410.13849>.
- [21] I. A. Ibragimov and R. Z. Has'minskii. *Statistical Estimation: Asymptotic Theory*. Springer, New York, 1981.
- [22] H. Jaeger. Short term memory in echo state networks. Technical Report GMD Report 152, Fraunhofer Institute for Autonomous Intelligent Systems, 2002.
- [23] S. Jastrzebski, Z. Kenton, D. Arpit, N. Ballas, V. Verma, K. Cheung, and Y. Bengio. Three factors influencing minima in SGD. In *ICLR Workshop*, 2017.
- [24] L. Jing, D. C. Gürsoy, T. Laurent, Y. LeCun, and Y. Bengio. Tunable efficient unitary neural networks (eunn) and their application to rnns. In *International Conference on Machine Learning*, 2017.
- [25] D. P. Kingma and J. Ba. Adam: A method for stochastic optimization, 2017. URL <https://arxiv.org/abs/1412.6980>.
- [26] J. Koutnik, K. Greff, F. Gomez, and J. Schmidhuber. A clockwork RNN. In *International Conference on Machine Learning*, volume 32, pages 1863–1871, 2014.
- [27] S. G. Krantz and H. R. Parks. *The Implicit Function Theorem: History, Theory, and Applications*. Birkhäuser, Boston, MA, 2003. doi: 10.1007/978-0-8176-8230-9.
- [28] K. Krishnamurthy, T. Can, and D. J. Schwab. Theory of gating in recurrent neural networks. *Physical Review X*, 12(1):011011, 2022. doi: 10.1103/PhysRevX.12.011011.
- [29] Q. V. Le, N. Jaitly, and G. E. Hinton. A simple way to initialize recurrent networks of rectified linear units. In *arXiv preprint arXiv:1504.00941*, 2015.
- [30] L. Le Cam and G. L. Yang. *Asymptotics in Statistics: Some Basic Concepts*. Springer, New York, 2000.
- [31] H. Li, Z. Xu, G. Taylor, C. Studer, and T. Goldstein. Visualizing the loss landscape of neural nets. *Advances in Neural Information Processing Systems*, 2018.
- [32] Z. Liu. Online convex optimization with heavy tails: Old algorithms, new regrets, and applications, 2025. URL <https://arxiv.org/abs/2508.07473>.
- [33] L. Livi. Time-scale coupling between states and parameters in recurrent neural networks. *arXiv preprint arXiv:2508.12121*, 2025. doi: 10.48550/arXiv.2508.12121. URL <https://arxiv.org/abs/2508.12121>.
- [34] I. Loshchilov and F. Hutter. Decoupled weight decay regularization. *International Conference on Learning Representations*, 2019.
- [35] J. Martens. New insights and perspectives on the natural gradient method. *arXiv preprint arXiv:1412.1193*, 2014.
- [36] S. McCandlish, J. Kaplan, and D. Amodei. An empirical model of large-batch training. *arXiv preprint arXiv:1812.06162*, 2018.

- [37] J. H. McCulloch. Simple consistent estimators of stable distribution parameters. *Communications in Statistics–Simulation and Computation*, 15(4):1109–1136, 1986.
- [38] J. P. Nolan. *Univariate Stable Distributions: Models for Heavy Tailed Data*. Springer Series in Operations Research and Financial Engineering. Springer, Cham, 2020. ISBN 978-3-030-52917-8. Print ISBN: 978-3-030-52917-8; eBook ISBN: 978-3-030-52918-5.
- [39] R. Pascanu, T. Mikolov, and Y. Bengio. On the difficulty of training recurrent neural networks. In *Proceedings of the 30th International Conference on Machine Learning*, volume 28, pages 1310–1318, Atlanta, Georgia, USA, 2013.
- [40] J. Pennington, S. Schoenholz, and S. Ganguli. Resurrecting the sigmoid in deep learning through dynamical isometry: theory and practice. In *Advances in Neural Information Processing Systems*, pages 4785–4795, 2017.
- [41] Y. Rubanova, R. T. Chen, and D. Duvenaud. Latent ordinary differential equations for irregularly-sampled time series. In *Advances in Neural Information Processing Systems*, 2019.
- [42] S. Ruder. An overview of gradient descent optimization algorithms. *arXiv preprint arXiv:1609.04747*, 2016.
- [43] A. M. Saxe, J. L. McClelland, and S. Ganguli. Exact solutions to the nonlinear dynamics of learning in deep linear neural networks. *arXiv preprint arXiv:1312.6120*, 2013.
- [44] R. Shwartz-Ziv and N. Tishby. Opening the black box of deep neural networks via information. *arXiv preprint arXiv:1703.00810*, 2017.
- [45] U. Simsekli, L. Sagun, and M. Gurbuzbalaban. A tail-index analysis of stochastic gradient noise in deep neural networks. In *Advances in Neural Information Processing Systems*, pages 1–12, 2019.
- [46] S. L. Smith and Q. V. Le. A bayesian perspective on generalization and stochastic gradient descent. In *International Conference on Learning Representations*, 2018.
- [47] C. Tallec and Y. Ollivier. Can recurrent neural networks warp time? In *International Conference on Learning Representations*, 2018.
- [48] A. W. van der Vaart. *Asymptotic Statistics*. Cambridge University Press, 1998.
- [49] P. Verzelli, C. Alippi, and L. Livi. Echo state networks with self-normalizing activations on the hypersphere. *Scientific Reports*, 9:13887, 2019. doi: 10.1038/s41598-019-50158-4.
- [50] S. Wisdom, T. Powers, J. R. Hershey, J. Le Roux, and L. E. Atlas. Full-capacity unitary recurrent neural networks. In *Advances in Neural Information Processing Systems*, 2016.
- [51] G. Yang and E. Hu. Tensor programs v: Tuning large neural networks via zero-shot hyperparameter transfer. In *Advances in Neural Information Processing Systems*, 2021.
- [52] C. Zhang, S. Bengio, and Y. Singer. Are all layers created equal? *Journal of Machine Learning Research*, 23(67):1–28, 2022.
- [53] J. Zhang, A. M. Saxe, M. S. Advani, and A. Lee. Improving the trainability of deep networks by standardizing the gradient. In *International Conference on Machine Learning*, 2020.
- [54] P. Zhou, J. Feng, C. Ma, C. Xiong, S. C. H. Hoi, and W. E. Towards theoretically understanding why SGD generalizes better than adam in deep learning. In H. Larochelle, M. Ranzato, R. Hadsell, M. Balcan, and H. Lin, editors, *Advances in Neural Information Processing Systems*, volume 33, pages 21285–21296. Curran Associates, Inc., 2020.